



UPPSALA
UNIVERSITET

*Digital Comprehensive Summaries of Uppsala Dissertations
from the Faculty of Science and Technology 1470*

Galactic archaeology with metal- poor stars

THOMAS NORDLANDER



ACTA
UNIVERSITATIS
UPSALIENSIS
UPPSALA
2017

ISSN 1651-6214
ISBN 978-91-554-9803-0
urn:nbn:se:uu:diva-313595

Dissertation presented at Uppsala University to be publicly examined in Polhemsalen, Ångströmlaboratoriet, Lägerhyddsvägen 1, Uppsala, Friday, 10 March 2017 at 13:15 for the degree of Doctor of Philosophy. The examination will be conducted in English. Faculty examiner: Professor David L. Lambert (The W. J. McDonald Observatory, Department of Astronomy, The University of Texas, Austin, TX 78712, USA).

Abstract

Nordlander, T. 2017. Galactic archaeology with metal-poor stars. *Digital Comprehensive Summaries of Uppsala Dissertations from the Faculty of Science and Technology* 1470. 73 pp. Uppsala: Acta Universitatis Upsaliensis. ISBN 978-91-554-9803-0.

The chemical fingerprints of old, metal-poor stars can be used to unravel the events of the newborn Universe and help us understand the properties of the first stars and star clusters. The study of nearby stars to infer properties in the distant past is often referred to as Galactic archaeology. However, the chemical composition of stars cannot be observed directly, but must be inferred by means of spectroscopic modelling. Traditionally, this modelling utilises one-dimensional (1D) stellar atmospheres in hydrostatic and local thermodynamic equilibrium (LTE). Today, we know that departures from LTE (known as NLTE), and differences between 1D model atmospheres and their hydrodynamical three-dimensional (3D) counterparts, become increasingly severe at lower metallicity. The development of NLTE modelling of spectral line formation in 3D atmospheres is still in its infancy, but constitutes a remarkable step forward that has been made possible by parallelised codes and supercomputers. The central theme of this thesis is the application of NLTE analyses to metal-poor stars, to help usher the field of Galactic archaeology forward with important consequences for the nature of the first stellar generations.

I present a theoretical NLTE study of aluminium, where I validate the analysis using a set of bright standard stars and provide calculated NLTE effects for a large parameter space. I perform 3D NLTE calculations for the solar spectrum to better constrain the zero-point of the cosmic abundance scale, and find excellent agreement with the meteoritic aluminium abundance.

I also present NLTE analyses of metal-poor stars in the globular clusters NGC 6397 and M4. While globular cluster stars were long expected to form from a chemically homogeneous medium, star-to-star abundance variations of light elements indicate multiple epochs of star formation. Massive first-generation stars polluted the interstellar medium from which later generations formed, and I use the observed abundance variations to deduce the properties of the polluting stars. Among the heavier elements, I uncover evolutionary abundance variations that match predictions of stellar evolution models with atomic diffusion. The results indicate that the chemical abundance ratios of unevolved metal-poor stars are affected by gravitational settling, with a bias of the order 25-50 %, increasing towards lower metallicity. This atmospheric depletion mechanism is a probable explanation to why the stellar abundances of lithium fall short of the predictions from standard Big Bang nucleosynthesis.

Finally, I apply a 3D NLTE abundance analysis to the red giant SMSS 0313-6708, which is the most iron-deficient star known. The chemical abundance pattern of this star indicates that it formed from gas affected only by Big Bang nucleosynthesis and a single faint supernova. Comparison of the inferred abundance pattern to theoretical predictions leads to constraints on the explosion mechanism and the mass of the metal-free progenitor star.

Keywords: stars: abundances, radiative transfer, stars: Population II, stars: Population III

Thomas Nordlander, Department of Physics and Astronomy, Observational Astronomy, 516, Uppsala University, SE-751 20 Uppsala, Sweden.

© Thomas Nordlander 2017

ISSN 1651-6214

ISBN 978-91-554-9803-0

urn:nbn:se:uu:diva-313595 (<http://urn.kb.se/resolve?urn=urn:nbn:se:uu:diva-313595>)

Till Jessica

Front cover image:

The granulation pattern in a hydrodynamical simulation of the ultra-metal poor red giant SMSS 0313-6708. The image illustrates the predicted variations in line strength across the surface, based on the 3D NLTE calculations for the Al I 3961 Å line presented in Paper IV of this thesis. Darker colours represent greater line strength, and the colour scale spans over nearly one order of magnitude.

List of papers

This thesis is based on the following papers, which are referred to in the text by their Roman numerals.

- I **Nordlander, T.** & Lind, K. (2017)
Non-LTE aluminium abundances in late-type stars
Astronomy & Astrophysics, submitted Jan. 2017
- II **Nordlander, T.**, Korn, A. J., Richard, O., & Lind, K. (2012)
Atomic Diffusion and Mixing in Old Stars. III.
Analysis of NGC 6397 Stars under New Constraints
The Astrophysical Journal, 753, 48
- III **Nordlander, T.**, Gruyters, P., Korn, A. J., & Richard, O. (2017)
Atomic Diffusion and mixing in old stars VII:
Chemical abundance variations in M4
To be submitted to Astronomy & Astrophysics
- IV **Nordlander, T.**, Amarsi, A. M., Lind, K., Asplund, M., Barklem, P. S., Casey, A. R., Collet, R., & Leenaarts, J. (2017)
3D NLTE analysis of the most iron-deficient star, SMSS0313-6708
Astronomy & Astrophysics, 597, A6

Reprints were made with permission from the publishers.

List of papers not included in the thesis

The following are publications to which I have contributed as author, but that are not included in this thesis.

1. **Nordlander, T.**, Rickman, H., & Gustafsson, B. (2017)
The Destruction of an Oort Cloud in a rich stellar cluster
Astronomy & Astrophysics, submitted Dec. 2016
2. Jönsson, H., Ryde, N., **Nordlander, T.**, Pehlivan, A., Hartman, H., Jönsson, P., & Eriksson, K. (2017)
Abundances of disk and bulge giants from hi-res optical spectra: I. O, Mg, Ca, and Ti in the Solar neighborhood and Kepler field samples
Astronomy & Astrophysics, in press
3. Frémat, Y., Altmann, M., Pancino, E., **et al.** (2016)
A test field for Gaia. Radial velocity catalogue of stars in the South Ecliptic Pole
Astronomy & Astrophysics, 597, A10
4. Gaia Collaboration, Brown, A. G. A., Vallenari, A., **et al.** (2016)
Gaia Data Release 1. Summary of the astrometric, photometric, and survey properties
Astronomy & Astrophysics, 595, A2
5. Gaia Collaboration, Prusti, T., de Bruijne, J. H. J., **et al.** (2016)
The Gaia mission
Astronomy & Astrophysics, 595, A1
6. Smiljanic, R., Romano, D., Bragaglia, A., **et al.** (2016)
The Gaia-ESO Survey: Sodium and aluminium abundances in giants and dwarfs. Implications for stellar and Galactic chemical evolution
Astronomy & Astrophysics, 589, A115
7. Hinkel, N. R., Young, P. A., Pagano, M. D., **et al.** (2016)
A Comparison of Stellar Elemental Abundance Techniques and Measurements
The Astrophysical Journal Supplement Series, 226, 4
8. Jofré, P., Heiter, U., Soubiran, C., Blanco-Cuaresma, S., Masseron, T., **Nordlander, T.**, Chemin, L., et al. (2015)
Gaia FGK benchmark stars: abundances of α and iron-peak elements
Astronomy & Astrophysics, 582, A81

9. Lind, K., Koposov, S. E., Battistini, C., **et al.** (2015)
The Gaia-ESO Survey: A globular cluster escapee in the Galactic halo
Astronomy & Astrophysics, 575, L12
10. Bergemann, M. & **Nordlander, T.** (2014)
NLTE Radiative Transfer in Cool Stars
in Determination of Atmospheric Parameters of B-, A-, F- and G-Type Stars, ed. E. Niemczura, B. Smalley, & W. Pych, *GeoPlanet: Earth and Planetary Sciences* (Springer International Publishing), 169–185
11. Bergemann, M., Ruchti, G. R., Serenelli, A., **et al.** (2014)
The Gaia-ESO Survey: radial metallicity gradients and age-metallicity relation of stars in the Milky Way disk
Astronomy & Astrophysics, 565, A89
12. Gruyters, P., **Nordlander, T.**, & Korn, A. J. (2014)
Atomic diffusion and mixing in old stars: V. A deeper look into the globular cluster NGC 6752
Astronomy & Astrophysics, 567, A72
13. Jofré, P., Heiter, U., Soubiran, C., **et al.** (2014)
Gaia FGK benchmark stars: Metallicity
Astronomy & Astrophysics, 564, A133
14. Smiljanic, R., Korn, A. J., Bergemann, M., **et al.** (2014)
The Gaia-ESO Survey: The analysis of high-resolution UVES spectra of FGK-type stars
Astronomy & Astrophysics, 570, A122

Contents

1 Galactic archaeology	11
1.1 Origin of the light elements	11
1.2 The first stars	13
1.3 Supernovae and the cosmic matter cycle	14
1.4 The formation of the Galaxy	19
1.5 Origin of the Galactic globular clusters	22
1.6 Challenges for Galactic archaeology	23
2 Stellar spectroscopy	27
2.1 Radiative transfer	27
2.2 The LTE case	28
2.3 The NLTE case	29
2.4 Non-LTE source function	30
2.5 Radiative transitions	31
2.6 Collisional transitions	33
2.7 Non-LTE mechanisms	36
2.8 Effects on line formation	37
2.9 The model atmosphere	39
2.10 3D radiative transfer	43
2.11 The necessity of 3D NLTE	45
3 Summary of papers	47
3.1 Paper I	47
3.2 Paper II	48
3.3 Paper III	50
3.4 Paper IV	51
4 Conclusions and outlook	53
4.1 Atomic diffusion	53
4.2 Beyond 3D NLTE	54
5 Contributions to the included papers	59
6 Svensk sammanfattning	61
7 Acknowledgements	65
References	67

1. Galactic archaeology

The prevailing theory of the history of the Universe is the so-called Λ CDM cosmology, which begins with the Big Bang. In the earliest times, a process named inflation caused space-time to expand exponentially until it was essentially flat, homogeneous, and isotropic. The Universe then evolved dynamically as described by the framework of general relativity in the presence of a cosmological constant (Λ) and cold dark matter (CDM). The ensuing structure formation has been modelled for large cosmological volumes in, e.g., the Millennium Simulation and its more recent incarnations (Springel et al. 2005; Angulo et al. 2012), and is illustrated in Fig. 1.1. Tracing the further evolution of the Universe using observations of long-lived nearby stars is known as Galactic archaeology. The key to its many successes lies in the stars' preservation of chemical and kinematical properties throughout cosmic time.

1.1 Origin of the light elements

After inflation had ended, the radiation-dominated Universe was still expanding rapidly and thus cooling off at a rate where $T \propto t^{-2}$. At early times, the Universe was hot enough that it consisted of a soup of fundamental particles in thermal equilibrium with the radiation, until after 10^{-6} s the temperature had decreased below 1 GeV (10^{13} K), and quarks coalesced to form protons and neutrons – collectively known as baryons.

As reviewed by e.g. Cyburt et al. (2016), the light elements formed during Big Bang nucleosynthesis (BBN) from chains of reactions like $p + n \rightarrow {}^2\text{H} + \gamma$, where protons and neutrons combine to form deuterium, which after further capture of a neutron and a proton produces ${}^4\text{He}$. However, the number of photons at a given energy E varies as $\eta^{-1} e^{-E/(kT)}$, where η is the baryon-to-photon number ratio (representing the cosmological density of baryons, Ω_b), and k the Boltzmann constant. Since the binding energy of deuterium is low, 2.2 MeV, and photons far outnumbered baryons by a factor 10^9 , the high-energy tail of photons destroyed any deuterium until the temperature dropped well below 1 MeV. The value of η thus determined the temperature (and time) when deuterium was no longer destroyed, at which point essentially all neutrons were used to form ${}^4\text{He}$.

In addition to hydrogen and helium, and their isotopes ${}^2\text{H}$ and ${}^3\text{He}$, small amounts of lithium were also produced, both indirectly by the dominant reaction ${}^3\text{He} + {}^4\text{He} \rightarrow {}^7\text{Be} + \gamma$, where ${}^7\text{Be}$ later decays to ${}^7\text{Li}$, and directly in

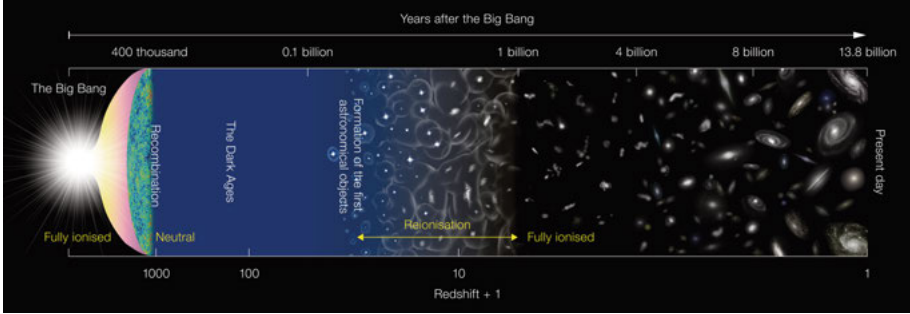


Figure 1.1. Timeline of the history of the Universe: After the Big Bang, the cosmic microwave background was produced during recombination. After hundreds of millions of years, the first stars and galaxies formed.

Image credit: ESO / NAOJ.

the ${}^3\text{H} + {}^4\text{He} \rightarrow {}^7\text{Li} + \gamma$ reaction. For a given cosmology, the relative abundances of these elements depend only on the nuclear reaction rates and the lifetime of free neutrons, which are measured in laboratory experiments, and the baryon-to-photon ratio η . Adopting $\eta \approx 6 \times 10^{-10}$, as measured from the cosmic microwave background (see below), calculations (e.g., Cyburt et al. 2016) yield a primordial composition of the Universe that is mainly ${}^1\text{H}$ and ${}^4\text{He}$ (75 % and 25 % by mass), as well as small fractions of ${}^2\text{H}$, ${}^3\text{He}$, and ${}^7\text{Li}$ (3×10^{-5} , 10^{-5} , and 4.7×10^{-10} relative to the number of ${}^1\text{H}$, respectively). The lithium abundance is often expressed on the customary logarithmic abundance scale as $A(\text{Li}) \equiv \log(n_{\text{Li}}/n_{\text{H}}) + 12 = 2.67 \pm 0.07$. By comparing these predicted yields to measurements of metal-poor stars and gas, we may test our understanding of the early Universe.

The primordial nucleosynthesis of the light elements took place within the first few minutes of the Big Bang, and for the following few hundred thousand years, the Universe consisted of radiation, free electrons, and light nuclei. It was opaque due to the large cross-section of Thomson scattering of photons on electrons, until at redshift $z \sim 1000$ when temperatures were sufficiently low that protons and electrons (re-)combined to form hydrogen atoms, so that photons finally decoupled from matter. The redshifted radiation from this time is observable today as the cosmic microwave background (CMB). Small spatial fluctuations in the temperature of these photons reveal the inhomogeneity of matter at the time of recombination and set the initial conditions for structure formation. The power spectrum of the fluctuations is used to determine η as well as other cosmological parameters in the ΛCDM framework (e.g., Planck Collaboration et al. 2016; see also the review by Samtleben et al. 2007).

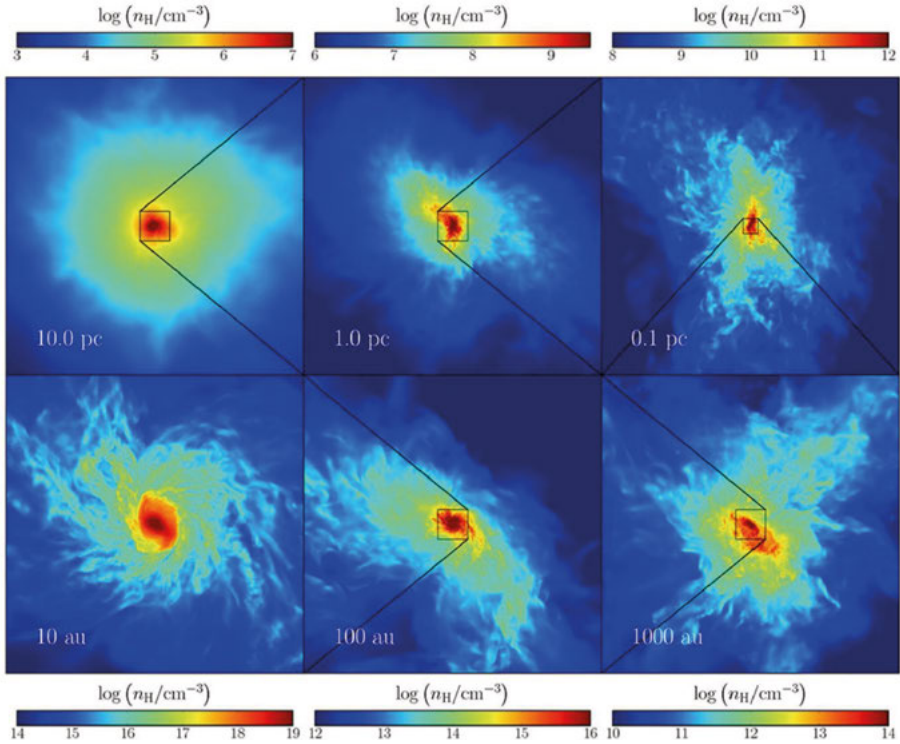


Figure 1.2. Simulation of the formation of the first stars, illustrating a zoom-in (clockwise order) from the massive self-collapsing minihalo to the protostar at the centre.

Image credit: Figure 1 of “Formation of massive protostars in atomic cooling haloes”, Becerra, F., Greif, T. H., Springel, V., & Hernquist, L. E. 2015, MNRAS, 446, 2380.

1.2 The first stars

Star formation requires a massive gas cloud to collapse under self-gravity. This leads to heating via adiabatic compression as well as shocks, which increases the pressure so that hydrostatic equilibrium halts further collapse. In order to continue, the surplus energy must be efficiently radiated away. In metal-rich gas clouds, this proceeds via the formation of CO and other molecules inside the cloud, with molecular association aided by the sublimation of gas onto dust grains (see the review by McKee & Ostriker 2007). The resulting mass distribution function can be seen, e.g., in the solar neighbourhood to be dominated by stars less massive than the Sun and drops off rapidly at higher mass (Salpeter 1955; Kroupa et al. 1993). In the early Universe however, the complete lack of metals and thus dust in the primordial composition made molecular formation inefficient. As the hydrogen molecule is homonuclear, it lacks rotational dipole transitions, which makes association via two-body collisions of neutral hydrogen atoms unlikely. It thus turns out that star formation in the early universe is a complicated and inefficient matter, where the cooling

processes favoured the initially high-temperature environments of very massive self-gravitating minihalos (see the review by Bromm 2013).

Cosmological simulations of star formation in the early universe indicate that the first stars, known as the Population III, were typically massive, in a broad range between $10 M_{\odot}$ and as much as $1000 M_{\odot}$ (e.g., Abel et al. 2002; Hirano et al. 2014). An example of the simulations by Becerra et al. (2015) is shown in Fig. 1.2, illustrating the large dynamical scales; the simulation covers over 20 orders of magnitude in gas density and 13 orders of magnitude in geometric distance.

These simulations are sensitive to the physics of accretion and radiative feedback, and a more accurate treatment of the radiative feedback reduces the highest achievable masses to about $300 M_{\odot}$ (Susa et al. 2014). These very massive stars formed either as singlets, or with a dominant massive star and a few lower-mass companions. In the large set of cosmological simulations by Hirano et al. (2015), the most massive stars formed early, at redshifts $z > 20$, while stars less massive than $50 M_{\odot}$ only formed at lower redshift when their less massive parent gas clouds had cooled sufficiently. The most massive stars produced large amounts of ionising radiation, which is believed to have played an important role for the reionisation of the Universe at an age of a few hundred million years (see Fig. 1.1).

High-resolution dynamical simulations by Greif et al. (2011) and Becerra et al. (2015) show that fragmentation in the accretion disk may instead have led to the formation of larger numbers of significantly less massive stars, perhaps no more than $0.1\text{--}10 M_{\odot}$. Their results imply the formation of a significant number of stars less massive than $0.8 M_{\odot}$ with lifetimes in excess of the age of the universe, which could in principle be observable today (e.g., Ishiyama et al. 2016). The fact that no true Population III star has yet been found in any spectroscopic survey may be used as a constraint on the lower mass limit of the first stars (e.g., Hartwig et al. 2015).

1.3 Supernovae and the cosmic matter cycle

After the epoch of Big Bang nucleosynthesis, stars have been responsible for producing the vast majority of all heavier elements in the Universe.

Depending on their mass, the first stars ended their lives in different ways. The calculations by Ezer & Cameron (1971) showed that the first stars were relatively compact and thus strongly gravitationally bound, since their complete lack of metals left them without an efficient means of burning hydrogen in their core. The proton-proton chains provided sufficient energy for protostars less massive than $10 M_{\odot}$, but at higher core temperature and pressure than in metal-rich stars. More massive protostars collapsed until temperatures and pressures in the core were sufficient to ignite helium burning in the

$3^4\text{He} \rightarrow ^{12}\text{C}$ process, producing small amounts of carbon which were then sufficient to burn hydrogen in the CN-cycle.

After 1–20 Myr, stars more massive than $10M_{\odot}$ would exhaust their hydrogen core and undergo further collapse until helium burning ignited again. The evolution following this point can be summarised as a sequence where the core burns helium to carbon, and continues to form oxygen, neon, magnesium, silicon, and so on up to iron and nickel. Because the core during these late stages of nucleosynthesis initially consisted entirely of helium, the α particles (i.e., ^4He nuclei) were the only building blocks available to form heavier elements. These are therefore known as α -elements, to indicate that their nuclei have even and equal numbers of protons (denoted by the atomic number Z) and neutrons. Similar chains of fusion processes occurred in burning fronts surrounding the core, so that these formed an onion-like structure where the outermost hydrogen-helium layers surrounded shells of successively heavier elements. Due to small amounts of hydrogen mixing into the burning shells surrounding the core, some odd- Z elements, such as ^{14}N , also formed.

Iron and iron-peak elements are the most strongly bound nuclei¹, and are therefore the end point of energy production by fusion as the synthesis of heavier elements would *absorb* energy instead of releasing it. The inert iron core of the massive stars therefore steadily increased in mass and contracted until electrons became degenerate. The end stages are unfortunately not clear for stars with masses in the range 10–100 M_{\odot} , because their explosion mechanism is not yet well understood. These core-collapse supernovae, regardless of the initial metallicity of the progenitor star, are known observationally as the Type II supernovae (SNe II). The general picture for SNe II, following the review by Burrows (2013), is that once the core mass surpasses the Chandrasekhar mass ($\sim 1.4M_{\odot}$), the electron degeneracy pressure is insufficient to halt collapse under self-gravity, and the core collapse proceeds during the course of less than a second. With the rapidly increasing core temperature, photons in the high-energy tail of their energy distribution become sufficiently numerous to photodisintegrate the iron nuclei, leaving a core consisting of ^4He and free neutrons, and later on even the ^4He nuclei are dissociated into protons and neutrons. At the same time, the rapidly increasing density leads to electron capture, $e^{-} + p \rightarrow n + \nu_e$, which acts as an electron sink and thus further decreases the degeneracy pressure and thus facilitates the collapse. This “neutronisation” process converts the inner core into a compact and degenerate proto-neutron star, whose stiffness causes the infalling outer parts of the core to bounce on its surface and reverse. This produces a shock wave, which heats and photodissociates the gas before stalling. Thus far, the process can in principle be modelled – but the star has not yet exploded, and the unresolved question is how the stalled shock is revived. A likely mechanism is

¹While ^{62}Ni has the highest binding energy per nucleon, the most strongly bound α -element is ^{56}Ni . However, it is unstable and its decay endpoint, ^{56}Fe , has the lowest mass per nucleon.

that this is facilitated by neutrinos: Earlier, the neutronisation process released large quantities of high-temperature neutrinos, that remained trapped inside the core until this stage when they escape and are absorbed by the outer core, thus reviving the shock and causing the supernova explosion.

Since the details of this mechanism are exceedingly difficult to model and its details thus largely unknown, the explosion is instead often parametrised by a piston action at an arbitrary location just outside the degenerate iron core, inserting a predetermined amount of energy of the order $1 B \equiv 10^{51} \text{ erg} = 10^{44} \text{ J}$. In the compact metal-free stars, this energy was likely only sufficient to eject the outermost layers, while the bulk of material fell back upon the neutron star or nascent black hole. This process, together with the suppression of light odd- Z elements, led to the particular abundance patterns of these faint “fall-back” supernovae. Their yields are predicted to have contained large amounts of carbon and oxygen, but only smaller amounts of heavier elements like calcium and iron (Heger & Woosley 2010). All SNe II, regardless of the metallicity of the progenitor star, produce ejecta that are rich in α -elements relative to iron. This is usually expressed such that the chemical composition is α -enhanced relative to Fe compared to the solar composition, or $[\alpha/\text{Fe}] > 0$, using the notation where $[X/Y] \equiv A(X) - A(Y) - (A(X)_{\odot} - A(Y)_{\odot})$.

In contrast to the SNe II, the explosion mechanism is well understood for metal-free stars more massive than $140 M_{\odot}$. These were presumably completely disrupted by an electron-positron pair instability, which led to exceedingly energetic so-called pair-instability supernovae (PISNe) with explosion energies as large as $80 B$. These produced large quantities of metals, in proportions that differed strongly from the solar pattern with characteristically low abundances of light as well as heavy odd- Z elements (Heger & Woosley 2002). Importantly, PISNe only occur for metal-free or low-metallicity progenitor stars.

Intermediate-mass stars in the range $1\text{--}8 M_{\odot}$ have lifetimes in the broad range 10 Myr to 10 Gyr and do not undergo core-collapse. Instead, they cease nuclear fusion after forming a core of carbon/oxygen or oxygen/neon. Their outer layers are lost in powerful winds and thermal pulsations as the star evolves to the asymptotic giant branch (AGB) where episodes of deep mixing bring processed material to the surface. Slow neutron captures on nuclei produce elements heavier than the iron-peak (where $Z \geq 38$; this is known as the s -process) and these elements are distributed by stellar winds (e.g., Herwig 2005; Karakas & Lattanzio 2014). After the AGB phase, only the inert and degenerate stellar core remains and is known as a white dwarf. In close binary systems, mass overflow from the lower-mass companion may increase the mass of the white dwarf above its stable limit, leading to detonation and thermonuclear runaway in a Type Ia supernova (SNe Ia). These occur on timescales of billions of years (e.g., Förster et al. 2006) and produce large amounts of iron (e.g., Nomoto et al. 1997).

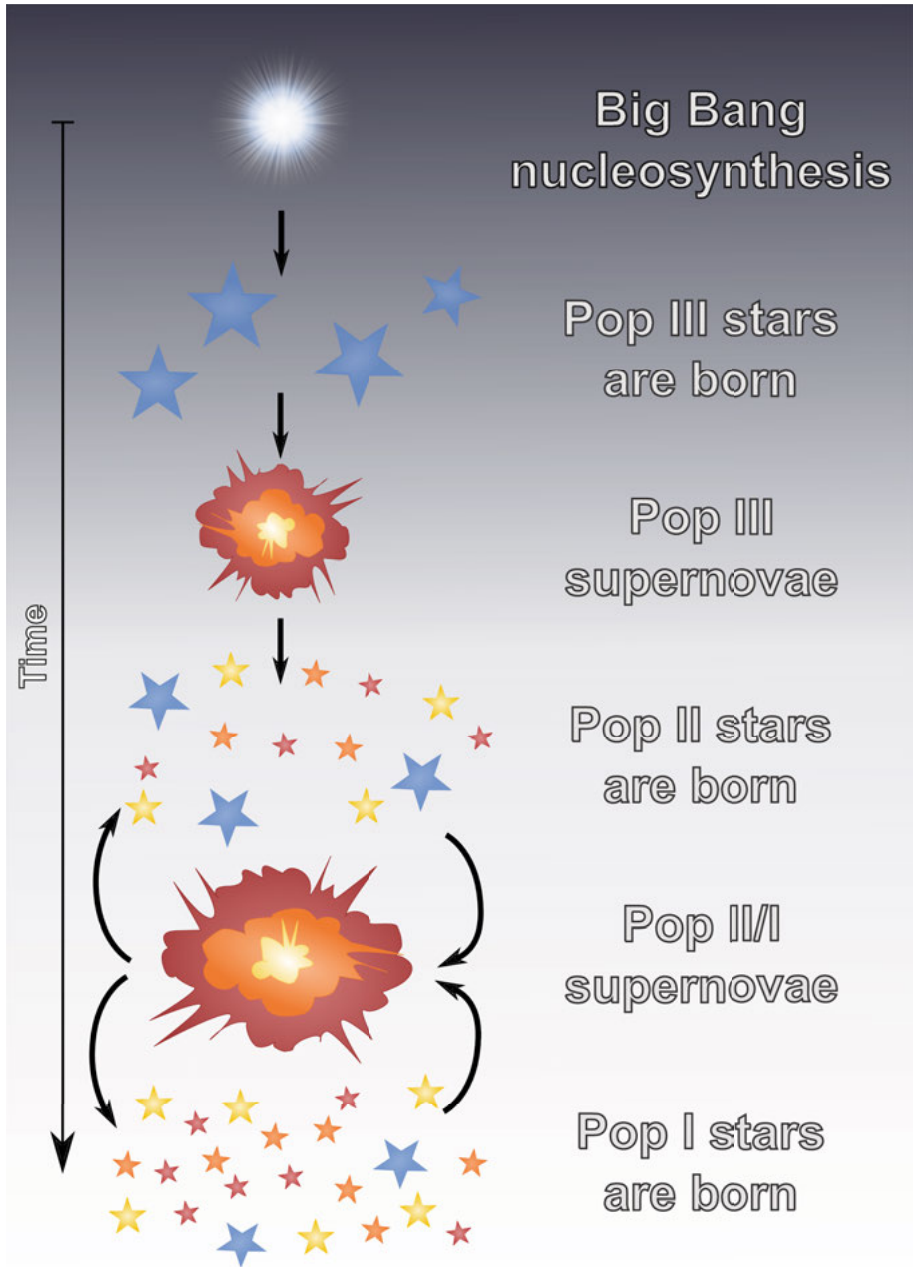


Figure 1.3. Sketch of the chemical enrichment of the Galaxy. The first elements were created in the Big Bang. Massive Population III stars exploded as the first supernovae, providing metals for the Population II stars and initiating the cosmic matter cycle: metals ejected by supernovae are incorporated into stars, which explode as supernovae, producing more metals.

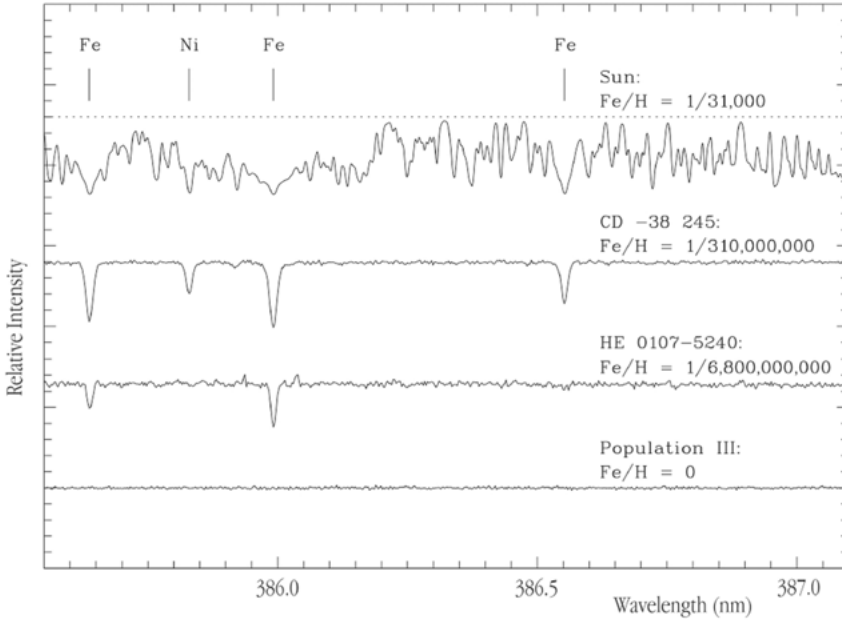


Figure 1.4. Comparison of spectra of stars with decreasing metallicity, ranging from the rich line spectrum of the Sun (top) to the hypothetical spectrum of a metal-free Population III star (bottom).

Image credit: ESO.

As the ejecta from the first supernovae mixed with the interstellar medium, it was enriched in metals. This allowed a different mode of star formation, with the cooling process now aided by dust grains, resulting in the characteristically lower-mass metal-poor Population II stars. The formation of these stars likely followed an initial mass function similar to that observed today, leading to large quantities of low-mass stars whose lifetimes exceed the current age of the Universe. The further evolution of these stars led to more SNe II and SNe Ia, which enriched the interstellar medium with metals, leading to the formation of more metal-rich stars and new generations of supernovae, where, e.g., the SNe II are characterised by lower stellar masses but higher explosion energies than in the early Universe. This process of the chemical enrichment of the Galaxy is known as the cosmic matter cycle, and is illustrated in Fig. 1.3. It forms the basis of Galactic archaeology, as the chemical abundance patterns imprinted on old stars in the solar neighbourhood can be used to determine the nucleosynthetic processes in stars in the distant past. The chemical abundances are measured from spectra, and an example of this is given in Fig. 1.4, for stars ranging from high to low and even zero metallicity.

1.4 The formation of the Galaxy

A plethora of evidence, including the rotation curves of external galaxies and observations of the CMB, supports the view that our Universe does not only consist of baryonic matter. The presence of an unknown type of non-luminous matter, termed dark matter, is required in an abundance several times larger than that of luminous matter. Various astrophysical arguments (e.g. the spatial scale of mass fluctuations) indicate that these particles are relatively massive ($> 10 \text{ GeV}$) and thus kinematically “cold”, in contrast to low-mass neutrinos or axions which would represent a form of hot dark matter. Hence, we use the term cold dark matter, or CDM. Observations of the CMB indicate that the Universe has very little curvature, and is consistent with it being flat. The expansion rate of the Universe has been measured using supernovae at large redshifts, indicating that it is in fact accelerating, which requires an additional energy component known as the cosmological constant, denoted Λ in the Friedmann equation (e.g., Perlmutter et al. 1999).

Dark matter does not interact electromagnetically, but only gravitationally and possibly through the weak force. Any small initial perturbations in the mass density left after inflation would thus be more easily amplified in dark matter. Not being hindered by radiation, dark matter clumped together to form large-scale structures earlier than baryonic matter. As discussed in the previous sections, cosmological simulations indicate that this clumping led to the formation of dark matter subhalos of mass $10^6 M_{\odot}$ wherein the first stars formed at redshifts $z \approx 20\text{--}30$ (Gao et al. 2007; Bromm 2013). An example of the present-day large-scale structure predicted by cosmological simulations (Vogelsberger et al. 2014) is illustrated in Fig. 1.5.

The formation of the Galaxy depicted by the Λ CDM cosmology is one of hierarchical structure, where the Galaxy formed and grew by the merger and accretion of dark matter subhalos (e.g., Tumlinson 2010). Similar-sized interacting subhalos merged completely and smoothly, while relatively smaller subhalos accreted as streams and may have survived as remnants in the larger halo. The Galaxy assembled from the inside out, such that the oldest subhalos were accreted early on, predominantly forming the central regions of the Galaxy known as the bulge, while the halo was built over longer timescales; in fact satellite accretion continues to the present day. The majority of very old stars are believed to be found in the bulge, but there they are much harder to find than in the less chemically evolved halo (see Howes et al. 2015). While stellar motions are essentially collisionless and stars therefore retain their birth orbits in terms of average orbital energy and angular momentum (only true to first order; see, e.g., Sellwood & Binney 2002), the gas components interact collisionally and thus evolve rapidly. In particular, a net angular momentum was retained during contraction of the gaseous halo, which thus flattened into a disk, while the stellar halo did not. The Galactic disk, which hosts our solar system, is the only component with active star formation today, a process that

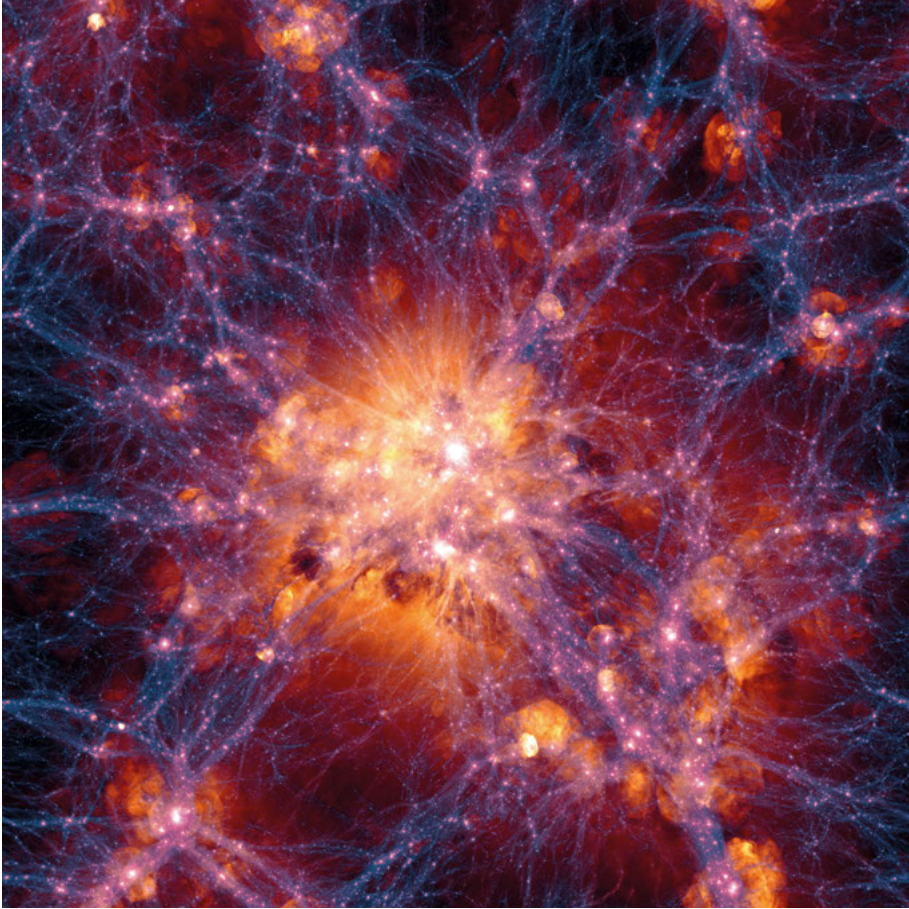


Figure 1.5. Illustration of the large-scale structure of the Universe, based on a cosmological simulation. Blue colours trace the distribution of dark matter, while orange represents gas – in this case, a massive galaxy cluster 100 Mpc across with prominent filamentary dark matter structure.

Image credit: ESO / Illustris Collaboration

is intimately linked to the passage of its prominent spiral arms. Stars in the disk have a large age spread, but are characteristically younger than the halo and bulge (e.g., Hayden et al. 2015).

The Galactic disk is often separated in two sub-components, although some authors argue for a unified view. Near the Galactic plane, most stars belong to the so-called thin disk, while stars located more than 1.5 kpc above or below the plane at the solar orbit belong to a second population known as the thick disk (Yoshii 1982; Gilmore & Reid 1983). While the thin disk is a natural consequence of the collapse of a gas disk, the formation of the thick disk is debated. Before the Λ CDM cosmology emerged, the monolithic collapse scenario dictated that stars in the thick disk formed as a late continuation of the halo as it collapsed to form the thin disk (e.g., Eggen et al. 1962; Larson 1974; Burkert et al. 1992). More in line with the inside-out formation scenario, the thick disk stars may have formed from multiple mergers during the build-up of the Galaxy (e.g., Brook et al. 2004, 2005) or been deposited as stellar streams during mergers (Abadi et al. 2003). Or, a pre-existing thin disk may have been dynamically heated, due to internal processes such as scattering by transient spiral arms or giant molecular clouds (e.g., Roškar et al. 2008), or during a minor merger (Quinn et al. 1993) which may also have left tidal streams (Villalobos & Helmi 2008).

Despite their varied origins, this plethora of suggested formation mechanisms often produce only subtly different predictions for the spatial distribution of thick disk stars. Additional constraints come from the ages of thick disk stars, with the caveat that these are usually not possible to determine to an accuracy and precision better than 10 % for field stars (Soderblom 2010). As discussed by Feltzing & Chiba (2013), the combination of kinematics, chemistry and ages may help distinguish between the formation scenarios outlined above.

In summary, the Galactic bulge, halo, and thick disk all give Galactic archaeology studies important clues about events that occurred at early times. Indeed, Tumlinson (2010) showed that among extremely metal-poor stars, the bulge region rather than the halo has the highest density of very old stars. However, the chemically pristine stars are vastly outnumbered here and also heavily obscured by interstellar gas and dust. This makes the old and metal-poor stellar halo the most accessible and undisturbed place to study the infant Universe.

The chemical fingerprints of the first stars are found in the most metal-poor stars, $[\text{Fe}/\text{H}] < -4$, which typically exhibit enhanced abundances of carbon and oxygen compared to iron, indicating that they formed from material that was ejected from low-energy SNe II (e.g., Frebel et al. 2008 and Paper IV). Similarly, metal-poor stars in the Galactic halo, bulge, and thick disk have enhanced abundances of α -elements, $[\alpha/\text{Fe}] > 0$, which is consistent with the ejecta of normal SNe II (e.g., Gehren et al. 2006; Ruchti et al. 2011; Bergemann et al. 2014). The chemical composition of thick disk stars is dis-

tinct from that of stars in the Galactic thin disk, including the Sun, where the lower $[\alpha/\text{Fe}]$ values indicate significant contribution from SNe Ia which we know occur on longer timescales than SNe II (e.g., Edvardsson et al. 1993; Fuhrmann 2004; Bensby et al. 2014).

While these results are broadly in agreement with the scenario for the formation of the Galaxy outlined above, there are other possibilities, not the least concerning the many scenarios for the formation of the Galactic thick disk and the build-up of the Galactic halo. For example, the nucleosynthetic sites are not necessarily settled, and it is not yet clear whether additional components are required, such as neutron star mergers, double-degenerate SNe Ia, and s-process contribution from rotating massive stars. Importantly, our understanding of the origin and evolution of the Galaxy and the enrichment of matter is observationally driven, and in line with the scientific spirit, the models yield verifiable and falsifiable predictions.

1.5 Origin of the Galactic globular clusters

The bulk of stars today form in clusters and associations with masses greater than $50 M_{\odot}$, with roughly equal numbers of stars contributed from clusters which formed 10^2 , 10^3 , and 10^4 stars (Lada & Lada 2003). These so called open clusters form from the collapse of giant molecular gas clouds in the Galactic disk and disperse or disintegrate entirely with time. Globular clusters (GCs), on the other hand, have estimated initial masses of 10^4 – $10^6 M_{\odot}$ and reside in the Galactic halo and bulge. They are the older (> 10 Gyr) and more massive analogues of the younger open clusters and were able to form because of higher gas pressures in the early Galaxy (Kruijssen 2015), or as a consequence of halo mergers and feedback (Bekki et al. 2008).

To first approximation, most GCs are single stellar populations, i.e. all stars are coeval and have homogeneous chemical composition. However, on closer inspection, all Galactic GCs examined to date exhibit characteristic abundance anomalies, where the (anti-)correlated abundance variations among the light elements may amount to as much as 1 dex, while the composition of heavy elements ($Z \gtrsim 14$) is indistinguishable from star to star (Gratton et al. 2012). These abundance patterns are unique to the high-density environments of GCs and indicate that they formed gradually, in one prolonged epoch or multiple distinct epochs of star formation. While first-generation stars exhibit pristine abundance patterns typical of the Galactic halo, later generations of stars formed out of material polluted by intermediate-mass or massive stars of previous generations. Different masses of polluting stars result in different characteristic abundance patterns of the second-generation stars. The observed properties of the GC stars, such as the magnitude of the abundance variations and the nucleosynthetic chains involved, may thus be used to infer the properties of the polluting stars and the initial mass of the GCs. The relative number

fractions of the pristine and polluted populations, and whether their chemical patterns are distinct or vary gradually, may be used to infer the formation time scale and the star formation efficiency.

In addition to tracing the early chemical and dynamical evolution of the Galaxy, GCs may also be used as laboratories for testing stellar evolution. One such case is introduced in the next section, and is used in Paper II and Paper III.

1.6 Challenges for Galactic archaeology

The chemical composition of stars cannot be directly measured but must be inferred using spectroscopic modelling. Traditionally, this modelling utilises one-dimensional (1D) stellar atmospheres and the assumption of local thermodynamic equilibrium (LTE). In the past decades, as three-dimensional (3D) stellar atmospheric models and the atomic data required to perform non-LTE (NLTE) calculations have become available, the shortcomings of the traditional techniques have become clear (see e.g. the reviews by Asplund 2005 and Bergemann & Nordlander 2014). Accurate atomic data for NLTE modelling is available only for a handful of elements, with the lack of accurate collisional transition data particularly troubling. Additionally, the interplay between NLTE effects and 3D atmospheric structures has only been explored in a handful of representative cases (e.g., Paper I and Paper IV). The modelling of stellar spectra is further described in Chapter 2.

Another complicating factor is that the present-day photospheric chemical composition of a star may differ from its initial composition. For example, accretion of metal-rich matter onto an initially metal-free stellar photosphere may disguise its chemical composition (e.g., Yoshii 1981; Frebel et al. 2009), and detailed calculations indicate that a characteristic abundance pattern should arise which is similar to that seen in certain extremely metal-poor stars (Johnson 2015). One must also consider a well-known and accepted evolutionary mechanism called the first dredge-up. This phenomenon occurs when the deepening surface convection zones of red giant stars reach layers that have been processed by nuclear reactions, where shell hydrogen burning in the non-equilibrium CNO cycle causes a net conversion of carbon to nitrogen.

Similarly, the surface abundance of lithium is known to become depleted on the subgiant branch (SGB) and red giant branch (RGB), because the convection zone reaches deep layers where lithium has been destroyed by proton capture reactions (e.g., Lind et al. 2009). This is particularly interesting, as lithium is one of few observables that may directly probe the very earliest state of the Universe via the yields from Big Bang nucleosynthesis. While the predicted cosmic abundance of lithium is $A(\text{Li}) = 2.67 \pm 0.07$ (Cyburt et al. 2016), observations of unevolved metal-poor stars on the so-called Spite

plateau (Spite & Spite 1982) indicate $A(\text{Li}) = 2.2$ (e.g., Asplund et al. 2006; Sbordone et al. 2010). This discrepancy by a factor 3, known as the cosmological lithium problem, would thus imply that either our understanding of the early Universe is in serious error, that spectroscopic modelling is significantly less accurate than previously thought, or that the chemical composition of the surfaces of unevolved stars do not represent their initial composition. Significant efforts have been spent attempting to find a solution in cosmology or in particle physics (see the review by Jedamzik & Pospelov 2009), and it was speculated that 3D NLTE effects may lead to significantly underestimated abundances (Kurucz 1995b). Early 3D LTE results implied that 3D modelling would seriously affect inferred abundances of lithium, but the abundance corrections were *negative* rather than positive, exacerbating the problem (Asplund et al. 1999). This is in stark contrast with 3D NLTE modelling, which was later found to be in close agreement with 1D NLTE results (Asplund et al. 2003; Barklem et al. 2003). Indeed, the observed abundances quoted above are derived from NLTE modelling, implying that the factor 3 discrepancy may be due to shortcomings in stellar evolution theory. This is not so far-fetched, since the solar lithium abundance is known to be depleted by at least 2 dex (e.g., Brun et al. 1999; Meléndez et al. 2010b).

A promising solution is that a process called atomic diffusion may cause element segregation in main-sequence stars, in particular in the radiative photospheres of early-type stars (which we do not discuss here) and below the surface convection zone of late-type stars (Michaud et al. 1984). Atomic diffusion represents a collection of microscopic mechanisms including gravitational settling, radiative levitation, and thermal diffusion, which cause a net migration of elements relative to hydrogen. Since the migration time scales are long, the mechanisms are particularly efficient when the convection zone is thin, as is the case for warm metal-poor stars. As the star evolves along the SGB and RGB, the surface convection zone grows thicker and reaches the deeper layers where matter has been deposited, so that it is brought back up to the surface. This process restores the initial chemical composition of all elements that have not been affected by nucleosynthesis in the dredged-up layers, i.e., lithium, carbon, and nitrogen are notable exceptions, and this is illustrated in Fig. 1.6 for a low-mass ($0.8M_{\odot}$), low-metallicity ($[\text{Fe}/\text{H}] = -1.1$) stellar evolution model. Calculations of these processes from first principles lead to very large surface abundance variations (up to an order of magnitude) in disagreement with observations, implying that additional mixing mechanisms are required (Richard et al. 2002b, 2005). Unfortunately the hypothesised processes, e.g., mixing induced by rotation and internal gravity waves (e.g., Charbonnel & Talon 2005; Talon & Charbonnel 2008), cannot currently be computed from first principles but rely on free parameters, which when calibrated to observed stars appear to vary with metallicity.

The question is, how does one determine whether a star has altered its surface chemical composition, when stellar lifetimes are measured in millions

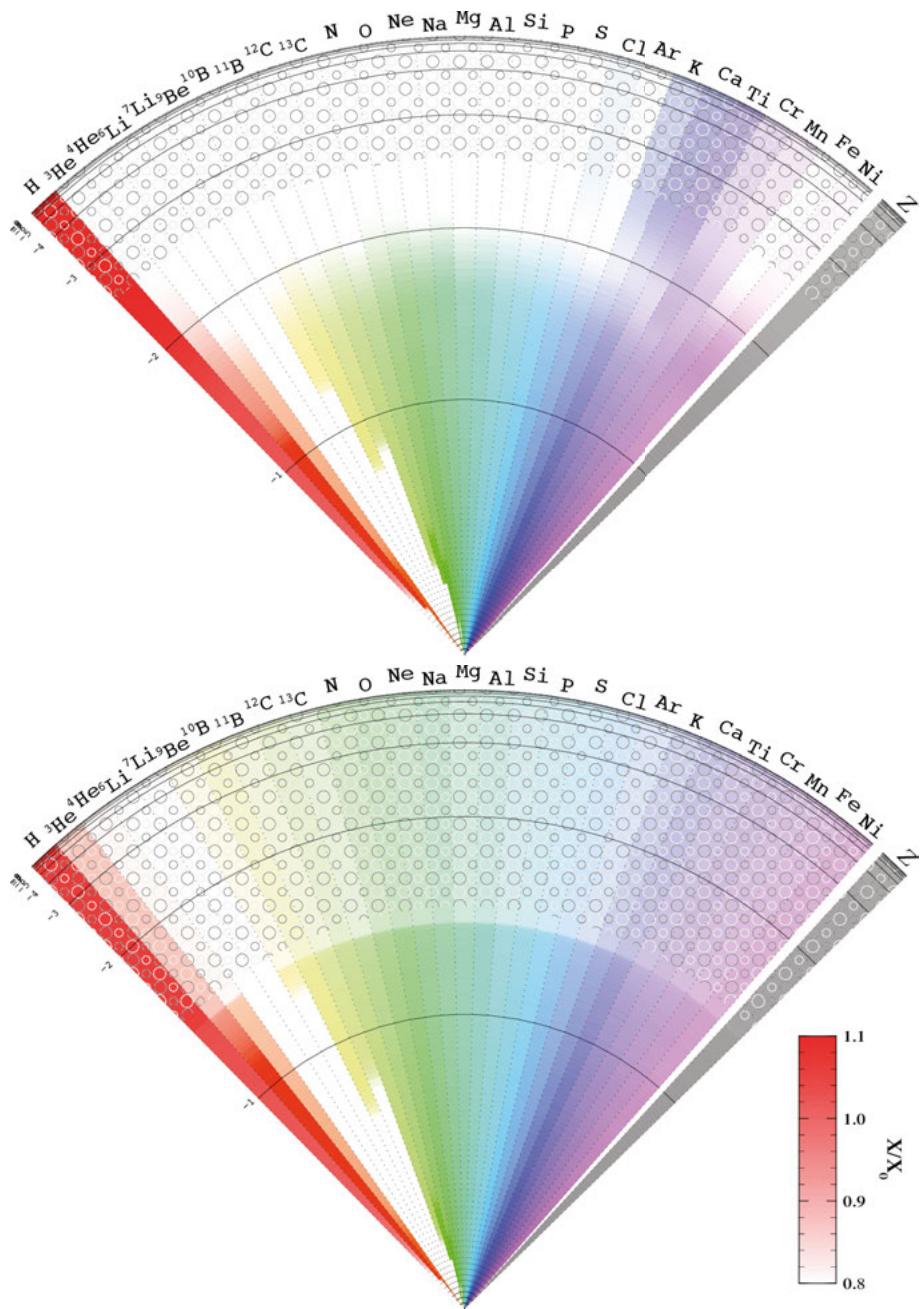


Figure 1.6. Illustration of the radial distribution of elements in a low-metallicity stellar evolution model, where darker colours indicate larger concentrations. The model is shown at the TOP (upper figure), when diffusion effects are largest, and on the SGB (lower figure), when the deep convection zone (bubbles) has nearly restored most surface abundances. Notably, lithium has been depleted throughout the star.

Image credit: Olivier Richard, priv. comm.

or billions of years? Rather than observe a single star as it evolves, one can observe stars expected to have had the same initial chemical composition but that differ in mass and therefore in their evolutionary state, e.g., stars in clusters or binary systems. Both these approaches have been used in the literature; in particular the ADiOS (Atomic Diffusion in Old Stars) series of papers, that focuses on studies of stars in the globular clusters NGC 6397 ($[\text{Fe}/\text{H}] = -2.1$; Korn et al. 2006, 2007; Lind et al. 2008, 2009; and Paper II), NGC 6752 ($[\text{Fe}/\text{H}] = -1.6$; Gruyters et al. 2013, 2014), M4 ($[\text{Fe}/\text{H}] = -1.1$; Paper III), and M30 ($[\text{Fe}/\text{H}] = -2.3$; Gruyters et al. 2016). These observations indicate that surface abundances of unevolved stars are affected on the level of 0.1–0.3 dex, with stronger effects at lower metallicity. This implies that the chemical composition of unevolved metal-poor field stars is distorted by an amount that varies from element to element and indeed from star to star. By selecting parametrised stellar evolution models that match observations best, it appears that additional mixing is significantly less efficient at lower metallicity. In particular, these models predict that the surface abundances of lithium in unevolved metal-poor stars are depleted by roughly 0.3 dex, almost enough to bridge the gap between stellar abundances and Big Bang nucleosynthesis.

It is important that the spectroscopic modelling underpinning these investigations is as accurate as possible, to ensure that the observed abundance variations are not spurious results of systematic errors. Additionally, the presence of multiple chemical populations must be taken into account, as these intrinsic abundance variations could otherwise be confused with evolutionary variations. The work presented in Paper II and Paper III therefore focuses on such difficulties, and utilises NLTE modelling. Tools for the NLTE modelling of aluminium are presented in Paper I, and a 3D NLTE analysis is presented in Paper IV. The theory behind spectroscopic 3D and NLTE modelling is presented in the next chapter.

2. Stellar spectroscopy

The science outlined in the previous chapter relies on being able to measure the chemical composition of stars. This is done by performing radiative transfer calculations in a pre-computed model atmosphere, and adjusting the chemical composition of the model until the synthetic spectrum matches the observed spectrum. In this chapter, we shall investigate what goes into these calculations, with a focus on deviations from local thermodynamic equilibrium (LTE), called non-LTE or NLTE.

2.1 Radiative transfer

The theoretical background of NLTE radiative transfer is given in detail in many textbooks, e.g., Rutten (2003) and Hubeny & Mihalas (2014). The application to cool stellar atmospheres was reviewed by Asplund (2005), and more recently by e.g. Bergemann & Nordlander (2014). A few central concepts are reviewed below following the notation of Rutten (2003). The discussion is limited to the case of complete frequency redistribution in bound-bound transitions and gas particle velocities following the Maxwell-Boltzmann distribution. Additionally, physical constants have their usual meaning, such as c representing the speed of light, h the Planck constant, and k the Boltzmann constant.

As the goal is to compute an emergent stellar spectrum, we begin with the radiative transfer equation, which describes the formation of the outgoing intensity I_ν along a ray with contributions from a source function S_ν . The equation and its formal solution can be formulated as

$$\frac{dI_\nu}{d\tau_\nu} = I_\nu - S_\nu \qquad I_\nu(\tau) = \int_{\infty}^{\tau} e^{-(\tau-t)} S_\nu dt, \qquad (2.1)$$

where $\tau_\nu = \int \rho \alpha_\nu ds$ is the optical depth along a path s (oriented outward) with density ρ and extinction coefficient α_ν .

In a one-dimensional plane-parallel geometry, the optical path can be evaluated along a ray with inclination θ relative to the normal axis. By defining a viewing angle $\mu \equiv \cos \theta$, the optical path then simply scales with $1/\mu$, resulting in an optical depth relative to the vertical, $d\tau_\nu(\mu) = d\tau_\nu(\mu = 1)/\mu$. In a horizontally inhomogeneous three-dimensional atmosphere, the intensity is evaluated by ray tracing, resulting in a quantity $d\tau_\nu(\vec{r}, \vec{l})$ at a point \vec{r} along a

ray \vec{l} . A reference optical depth, e.g. τ_{500} representing the continuum optical depth at $\lambda = 500$ nm, is typically defined along the vertical axis rather than as an angular average, even in an inhomogeneous structure. This has practical advantages, as it would otherwise be expensive to compute and would depend on the angular quadrature employed.

For the Sun, I_ν can be observed directly in resolved images of the surface. This is generally not the case, as all other stars are essentially point sources on the sky. The radiation we observe is then the flux $F_\nu \equiv \int I_\nu \cos \theta \, d\Omega$, or $F_\nu = 2\pi \int \mu I_\nu \, d\mu$ in the plane-parallel case, which is the emergent (line-of-sight) intensity averaged over all angles, representing a star projected on the plane of the sky. Another useful quantity is the mean intensity, $J_\nu \equiv \frac{1}{4\pi} \int I_\nu \, d\Omega$ or $J_\nu = \frac{1}{2} \int I_\nu \, d\mu$ in the plane-parallel case, which is simply the average of the intensity over all angles.

The source function in Eq. (2.1) is a combination of all relevant continuous processes and lines,

$$S_\nu = \frac{\sum \alpha_\nu^c S_\nu^c + \sum \alpha_\nu^l S_\nu^l}{\sum \alpha_\nu^c + \sum \alpha_\nu^l} \quad (2.2)$$

where α_ν^c and α_ν^l represent the extinction coefficients of all continuous processes and lines, respectively, and S_ν^c and S_ν^l their source functions. The extinction coefficient can be written as $\alpha_\nu = n\sigma_\nu$, where n is the population of the initial state, and σ_ν the cross-section per particle. The line source function for a transition $i \rightarrow j$ with frequency ν can be expressed as

$$S_\nu^l = \frac{2h\nu^3}{c^2} \frac{1}{\frac{g_j n_i}{g_i n_j} - 1}, \quad (2.3)$$

where g_i the statistical weight of the lower level i of the transition, and n_i its population.

With these definitions, solving the radiative transfer equation requires knowledge of the extinction coefficients α_ν and source functions S_ν . These can be computed if the thermodynamic variables of a model atmosphere are known. Solving the equation of state yields the concentrations of different chemical species, and α_ν and S_ν are then computed using lists of atomic and molecular lines and continua. The missing ingredient concerns the energy partitioning among the atomic and molecular states available for each chemical species.

2.2 The LTE case

Under the commonly made assumption of LTE, the energy partitioning can be computed analytically as a function only of *local* thermodynamic variables.

The Boltzmann equation describes the partitioning of energies among excited states of a chemical species,

$$n_i^* \propto g_i e^{-\chi_i/kT} \quad (2.4)$$

where n_i^* is the LTE population of a state i with excitation energy χ_i . Similarly, the Saha equation describes the degree of ionisation,

$$\frac{n_{r+1}^* n_e}{n_r^*} \propto \frac{U_{r+1}}{U_r} (kT)^{\frac{3}{2}} e^{-\chi_r/kT}, \quad (2.5)$$

where n_r is the relative population of the stage r with ionisation potential χ_r relative to the next higher stage $r + 1$. The partition functions U_r and U_{r+1} are summations of Eq. (2.4), and n_e is the number density of electrons.

Inserting Eq. (2.4) for a transition $i \rightarrow j$ with energy $\chi_j - \chi_i = h\nu$ into the line source function, Eq. (2.3), we find

$$S_\nu^l = \frac{2h\nu^3}{c^2} \frac{1}{e^{h\nu/kT} - 1} = B_\nu, \quad (2.6)$$

where B_ν is the Planck function. The line source function thus depends only on the local temperature and the frequency of the transition, and requires no further knowledge of the chemical species involved.

2.3 The NLTE case

In the transparent layers of stellar atmospheres, conditions are often such that LTE is not fulfilled. More generally, the population n_i of an atomic level i may be computed from the time-independent equations of statistical equilibrium,

$$0 = \frac{dn_i}{dt} = \sum_{j \neq i} n_j (R_{ji} + C_{ji}) - n_i \sum_{j \neq i} (R_{ij} + C_{ij}), \quad (2.7)$$

where R_{ij} and C_{ij} are the radiative and collisional rates for a transition $i \rightarrow j$. The first sum describes the incoming (populating) rates from every level j to the level i , and the second sum describes the outgoing (depopping) rates from the level i to every level j .

The radiative transition rates can be expressed as

$$R_{ij} = \int_0^\infty \frac{4\pi}{h\nu} \sigma_{ij}(\nu) J_\nu d\nu$$

$$R_{ji} = \int_0^\infty \frac{4\pi}{h\nu} \sigma_{ij}(\nu) \frac{n_i^*}{n_j^*} e^{-h\nu/kT} \left(\frac{2h\nu^3}{c^2} + J_\nu \right) d\nu, \quad (2.8)$$

where R_{ij} may denote an excitation (bound-bound) or dissociation (bound-free) transition, and R_{ji} a deexcitation or recombination transition. The cross-sections $\sigma_{ij}(\nu)$ describe either spectral lines or continuous processes.

For bound-bound transitions, i.e. spectral lines, the radiative rates may be expressed as

$$R_{ij} = B_{ij}\bar{J}_\nu \qquad R_{ji} = A_{ji} + B_{ji}\bar{J}_\nu, \qquad (2.9)$$

where we use the Einstein coefficients (rates) A_{ji} for *spontaneous* deexcitation, and B_{ji} and B_{ij} for *induced* deexcitation and radiative excitation. The induced radiative processes depend on $\bar{J}_\nu \equiv \int J_\nu \phi(\nu) d\nu$, which is the mean intensity for the transition at frequency ν averaged over its line profile $\phi(\nu)$. The Einstein coefficient A_{ji} is related to the oscillator strength $g_i f_{ij} = g_j f_{ji} \propto g_j A_{ji} \lambda^2$, and similar expressions exist for the other Einstein coefficients. The usefulness of equation (2.9) is thus that it embeds the line profile in the mean radiation field \bar{J}_ν , and instead illuminates the dependence on line strength: stronger transitions have larger radiative rates.

As the Boltzmann distribution and Planck function are convenient starting points, we can define departures from LTE using so-called departure coefficients,

$$\beta_i \equiv n_i/n_i^*, \qquad (2.10)$$

where n_i^* is the LTE population of state i . In LTE, $\beta_i = 1$ by construction.

2.4 Non-LTE source function

The line source function can be defined using departure coefficients,

$$S_\nu^l = \frac{2h\nu^3}{c^2} \frac{1}{\frac{\beta_i}{\beta_j} e^{h\nu/kT} - 1} \qquad (2.11)$$

$$\approx \frac{\beta_j}{\beta_i} B_\nu \qquad \text{if } h\nu \gg kT \qquad (2.12)$$

where the approximation is valid at optical and shorter wavelengths, where frequencies are sufficiently high¹ that $h\nu \gg kT$ at temperatures typically found in stellar atmospheres. This means that the contribution from stimulated emission can be neglected, which simplifies the Planck function to Wien's approximation, and for the non-LTE case results in Eq. (2.12). This simplified relation implies that a relatively increased population in the upper level results in a correspondingly brighter source function, and vice versa.

¹The numerical constant $h/k \approx 4.8 \times 10^{-11}$ s K. Substituting $\nu = c/\lambda$, the numerical constant corresponds to a wavelength of 2.9 μm at $T = 5000$ K.

In the infrared, as $h\nu$ becomes larger than kT , the Boltzmann factor $e^{h\nu/kT}$ will consequently approach 1. When the Boltzmann factor $e^{h\nu/kT} \approx \beta_j/\beta_i$, the denominator of Eq. (2.11) becomes very small, which in turn leads to a very large source function. Hence, due to stimulated emission in the infrared, a relatively increased population in the upper level leads to a much brighter source function relative to LTE, than the same situation for a transition in the optical. Such a case is investigated in Paper I (Chapter 3.1).

Returning to the source function, the total extinction coefficient α_ν represents a sum of processes where a photon may either be destroyed and reemitted thermally (true absorption) or emitted anew in a new direction (isotropic coherent scattering). It is illustrative to define a destruction probability $\varepsilon_\nu \equiv \alpha_\nu^{\text{abs}}/(\alpha_\nu^{\text{abs}} + \alpha_\nu^{\text{scat}})$, as the source function can then be expressed in terms of a local part and a non-local part,

$$S_\nu = (1 - \varepsilon_\nu)J_\nu + \varepsilon_\nu B_\nu. \quad (2.13)$$

This expression can be used whether we are discussing scattering in lines, or continuous processes, e.g. Rayleigh scattering on H I or Thomson scattering on free electrons. Further, it can be used in a regime between LTE and NLTE, where a non-local source function is used together with LTE level populations.

The classical case is that of continuous Rayleigh scattering in the UV. In one-dimensional LTE model atmospheres, the temperature declines monotonically with increasing height. At short wavelengths in the Wien regime, $B_\nu \propto \nu^3 e^{-h\nu/kT}$ decreases rapidly with decreasing temperature, giving the source function a very steep gradient. The radiation field J_ν is dominated by the contribution from deeper, hotter layers, and is much brighter than the local Planck function at short wavelengths. At the same time, Rayleigh scattering has a strongly wavelength dependent cross-section that varies as $\sigma \propto \nu^4$, and thus also increases rapidly at short wavelengths. In the UV, the combination of significant continuous scattering relative to true absorption (low ε_ν) and a superthermal radiation field ($J_\nu > B_\nu$), leads to a superthermal continuum source function ($S_\nu > B_\nu$). The continuum flux brightens and spectral lines are strengthened even without considering additional effects on the line source functions.

2.5 Radiative transitions

The solution of the statistical equilibrium equation (Eq. 2.7) depends on the relative strengths of radiative and collisional transitions. The radiative transition rates for all continua and lines are computed from Eq. (2.8), which require knowledge of both atomic transition data (σ_{ij}) and the radiation field (J_ν). Because the radiation field depends on the source function, which in turn depends on the level populations, the statistical equilibrium and radiative transfer equa-

tions need to be solved iteratively. The accuracy of the solution depends on the quality of the atomic data.

For bound-free transitions between some state i and a state j in a different ionisation stage, we require frequency-dependent cross-sections $\sigma_{ij}(\nu)$. These have an edge at the threshold frequency ν_0 corresponding to the energy difference between the two states, $h\nu_0 = \chi_j - \chi_i$. At higher frequencies, i.e. higher photon energies, a photoionisation event will leave the residual $\Delta E = h\nu - h\nu_0$ imparted as kinetic energy on the freed electron. While these cross-sections can be calculated exactly for hydrogen and hydrogenic atoms, no exact analytical solution generally exists for complicated electronic systems. Instead, laboratory data (when possible) and advanced numerical methods such as the close-coupling approximation are used in the literature (e.g. Cunto et al. 1993).

For bound-bound transitions, the cross-section $\sigma_{ij}(\nu)$ describes a transition probability distributed over a line profile. The strength is usually expressed in terms of oscillator strengths $f_{ij} \propto \int \sigma_{ij}(\nu) d\nu$. These transition probabilities are available in exact analytical form for hydrogen and hydrogenic states of other atoms, but must be computed numerically or measured in the laboratory for other electronic configurations.

The second component to σ_{ij} is the line profile. Due to various microscopic and macroscopic processes, line profiles are not sharp delta functions but have finite widths. First, natural broadening (or radiative damping) results in a Lorentzian profile, and is due to the finite lifetimes of excited states. Second, Doppler broadening due to local thermal motions result in a Gaussian profile. In addition, elastic collisions with charged or neutral particles perturb the electron structure of the atom. For metal lines, these processes also have Lorentzian shapes, and their widths are simply added to that of natural broadening (which is usually very small). Of particular interest and difficulty is broadening due to collisions with neutral hydrogen, commonly referred to as Van der Waals broadening and implemented using the analytical theory of Unsöld (1955). As reviewed by Barklem (2016a), this theory underestimates the influence of short-range interactions and thus yields damping constants too small by factors of a few. In contrast, the so-called Anstee-Barklem-O'Mara (ABO) theory (Anstee & O'Mara 1991) has proven to yield accurate line widths due to collisional broadening, with no need for astrophysical calibrations (see the examples given by Anstee & O'Mara 1995; Barklem & O'Mara 1998; Barklem 2016a). The Lorentzian and Gaussian profile contributions are convolved to form the generic Voigt profile of spectral lines. In addition to the mentioned microscopic broadening agents, large-scale velocity fields that arise due to convection and rotation imprint further Doppler broadening on the intrinsic Voigt profile, without changing the overall line strength.

Large consistent sets of radiative transition data commonly used are those of Kurucz (1995a) and the Opacity Project (Cunto et al. 1993). Both laboratory

and theoretical data are compiled by NIST ASD² (Reader et al. 2012) and VALD³ (Piskunov et al. 1995; Ryabchikova et al. 2015).

2.6 Collisional transitions

Collisional transitions are mainly due to interactions with free electrons and neutral hydrogen atoms. While electrons have low masses and thus high thermal velocities, hydrogen atoms are orders of magnitude more numerous in the line forming layers of stellar atmospheres, but due to their high mass have smaller thermal velocities. Historically, the importance of hydrogen collisions has been overlooked, because of their lower impact rates and the naive expectation that collisions are adiabatic, i.e. have small inelastic cross-sections (Massey 1949). Essentially, the electrons in the target atom have time to adjust during the interaction, which would make the transition unlikely.

The commonly used classical semi-empirical formalism of Drawin (1968) and Steenbock & Holweger (1984) describing hydrogen collisional transition rates is nowadays known to often be in error by orders of magnitude. In practice, these transition rates are commonly rescaled by a factor S_H , which varies from element to element and from author to author (see e.g. Table 2 of Bergemann & Nordlander 2014). The literature contains values ranging from 30 to 0.001 and even 0 (i.e., neglecting hydrogen collisions), where sometimes even different analyses of the same element have used as different scaling factors as 1 and 0. Some authors even implemented more advanced scaling relations, e.g., an exponential function ranging from 1 for low-excitation to 10^{-8} for high-excitation states of magnesium (Zhao et al. 1998). One explanation for why the scaling factors may differ strongly between authors despite their analyses yielding similar results, is that the empirical calibration to stellar spectra also compensates other, unrelated shortcomings. These may include uncertainties in the electron collisional transition rates, inaccuracies in radiative transition data, and incomplete term diagrams.

As reviewed by Barklem et al. (2011), the shortcoming of Drawin's formula when applied to hydrogen collisions is that it is based on an inappropriate physical description of electron impact ionisation, and thus assumes that the electron structure of the projectile remains static during the interaction. From quantum mechanical calculations, it is clear that the nucleus of the perturbing atom is involved in the interaction, which is quantum mechanical in nature. The result is that not only are the estimated transition rates generally overestimated by a few orders of magnitude, but they also exhibit scatter of a few orders of magnitude in comparison to quantum mechanical calculations.

²A compilation of compilations, available online at http://physics.nist.gov/PhysRefData/ASD/lines_form.html as well as in numerous published compilations.

³Available online at <http://vald.astro.uu.se>

Fortunately, accurate calculations of hydrogen collisions with several elements are now available. In a series of papers, quantum dynamical calculations of cross-sections (Belyaev & Barklem 2003; Belyaev et al. 2010, 2012) and transition rates (Barklem et al. 2003, 2010, 2012) have been computed for lithium, sodium, and magnesium. Larger systems are too complex for such calculations, which already for these relatively simple atoms require years of work. Instead, approximate methods have been developed (Belyaev 2013b; Barklem 2016b) and shown to provide accurate order-of-magnitude estimates of the partial processes with largest cross-sections that dominate the interactions. These methods have been applied to helium, beryllium, aluminium, silicon, calcium, and iron (Belyaev 2015; Yakovleva et al. 2016; Belyaev 2013a; Belyaev et al. 2014, 2016; Barklem 2016b; Nordlander et al. 2017a).

Both the quantum dynamical and approximate models are based on calculations for the hydride quasi-molecule formed during the $A + H$ interaction, where at short internuclear distances an electron tunnels over to form the ionic configuration $A^+ + H^-$, and so these are only applicable to bound states below the $A^+ + H^-$ ionic limit, 0.754 eV below the ionisation limit. The ionic configuration produces non-adiabatic couplings and thus greatly increases bound-bound transition probabilities compared to purely adiabatic transitions, because the electron may tunnel to the hydrogen atom and back. After the electron has tunnelled over to the hydrogen atom, it may simply remain there in a so-called charge transfer process, $A + H \rightarrow A^+ + H^-$, which has much larger cross-sections than the classical ionisation process $A + H \rightarrow A^+ + H + e$ (see, e.g., Barklem 2016a).

More highly excited Rydberg states can be treated by the free electron model of Kaulakys (1991), which is implemented in a freely available code by Barklem (2016c). These rates are typically significantly smaller than those computed with Drawin's formula, and in the case of magnesium are not too different from the relation calibrated by Zhao et al. (1998), mentioned above. While the free electron model can in principle be computed for any transition between any states, Barklem et al. (2011) note that for low-excitation states, its performance is in fact no better than the Drawin formula.

The relative importance of hydrogen atoms and electrons is estimated in Fig 2.1 for three representative stellar models in a range of metallicities. The upper panels illustrate the densities of ground-state hydrogen atoms and free electrons as a function of continuum optical depth in the model. As a rule of thumb, weak optical lines and the wings of strong lines form at large optical depths, $\log \tau_{500} \gtrsim -1$, while the cores of stronger lines form farther out. At large optical depth, hydrogen and electron densities are comparable to within a few orders of magnitude. Farther out, hydrogen densities decrease slowly while electron densities decrease rapidly. At lower metallicity, the ratio of number densities between hydrogen atoms and electrons increases, as metals are electron donors. Hydrogen atoms thus appear to be increasingly important at smaller optical depths and low metallicity. Additionally, hydrogen atoms

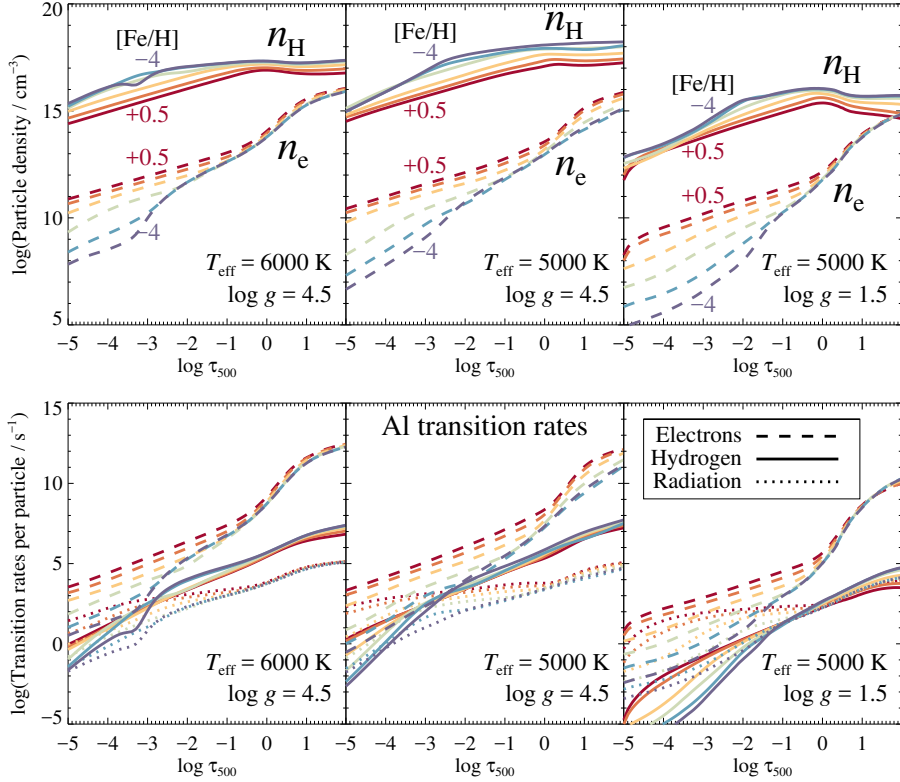


Figure 2.1. Particle densities (top) and aluminium transition rates (bottom) in three types of stars (parameters in each frame) with varying metallicity (represented by colour, labelled in the top plot). Densities and rates are illustrated for hydrogen atoms (n_{H} , solid lines), electrons (n_{e} , dashed lines) and radiation (dotted lines; rates only). The transition rates are given per aluminium atom.

appear more important in cooler models and at lower surface gravity, where all densities are lower.

The relative influence will depend on the chemical species being studied, but we take aluminium as an illustrative example using data from Nordlander & Lind (2017, Paper I, see Chapter 3.1). The lower panels of Fig. 2.1 illustrate the total transition rates due to collisions with electrons and hydrogen atoms, as well as the radiative rates. All states of aluminium are included in the summation, but fine structure transitions and excitations in Al II are ignored. The collisional rates are the sum of excitations and ionisations (for electrons) and charge transfer (for hydrogen atoms). In all models, electrons clearly dominate at large optical depths, while hydrogen atoms become relatively more important toward smaller optical depth, and in particular at lower metallicity. At small optical depths, low surface gravity, and high metallicity, radiative rates become comparable to the collisional rates. In particular, large *imbalances*

in the radiative transition rates may drive large deviations from LTE. While these illustrations show a comparison of the total transition rates among all states in aluminium, the numbers tend to be dominated by a few transitions with very large rates. Understanding the detailed behaviour requires detailed investigation of relative rates, and how they influence individual states.

2.7 Non-LTE mechanisms

In general terms, departures from LTE occur when radiative rates are comparable to or larger than collisional rates. Scattering then becomes important relative to true absorption, i.e. when atoms have time to reemit photons before the energy is redistributed by collisions. This implies a very small destruction probability, $\varepsilon \approx 0$, and thus $S_v^l \approx \bar{J}_v$. As the radiation field determines the source function, by extension (Eq. 2.11) it will also determine the ratio of departure coefficients. In the Wien regime, Eq. (2.12), the effect on departure coefficients is simply $\bar{J}_v/B_v \approx S_v^l/B_v \approx \beta_j/\beta_i$. This case is typically, but not exclusively, found for strong lines coupled to the ground state, and is therefore known as *resonance scattering*. As the line strength grows, the line radiation field darkens to lower values, to less than the Planck function, causing the upper level to become depopulated relative to the lower level. The effect is typically stronger in the infrared where $J_v < B_v$ is often already the case.

At UV wavelengths, the radiation field is instead superthermal, $J_v > B_v$, and the upper levels involved in line transitions become overpopulated relative to the lower level, $\beta_j > \beta_i$. For bound-bound transitions, this process is known as *photon pumping*, or *over-excitation*.

The corresponding bound-free effects are referred to as over-recombination and over-ionisation, corresponding to the cases of subthermal and superthermal radiation fields of ionising photons, respectively. Neutral species are typically in minority with respect to singly ionised species by one to three orders of magnitude in late-type stellar atmospheres. Any imbalance caused by a non-thermal radiation field will thus have much larger impact on neutrals.

The collisional Einstein coefficients C_{ij} and C_{ji} are related by the concept of detailed balance, i.e. thermodynamic equilibrium. This concept states that the sum of transition rates between any two states is exactly equal in both directions, so that

$$n_i^* C_{ij} = n_j^* C_{ji}. \quad (2.14)$$

If a collisional transition $i \rightarrow j$ locally dominates the system of equations, then the relevant parts of Eq. (2.7) reduce to $n_i C_{ij} = n_j C_{ji}$. Rearranging and identifying the collisional coefficients with Eq. (2.14), we find

$$\frac{n_i}{n_j} = \frac{C_{ji}}{C_{ij}} \equiv \frac{n_i^*}{n_j^*} \equiv \frac{g_i}{g_j} e^{(\chi_j - \chi_i)/kT}, \quad (2.15)$$

where the final equality uses the Boltzmann equation, Eq. (2.4). Consequently, we find that the *ratio* of level populations is in LTE, and $\beta_i = \beta_j$. The *absolute* populations may however deviate from LTE, so that $\beta_i = \beta_j \neq 1$.

2.8 Effects on line formation

Deviations from LTE thus depend in an intricate way on the balance between collisional and radiative transitions. This balance controls the level populations, which in turn control the line opacity as well as the line source function. In a nutshell, the line opacity determines the depth in the model atmosphere where the radiation originates – an increase in line opacity tends to shift the formation depth outward. The line source function describes the intensity originating at that depth, and thus determines the line depression – an increase in the source function at that depth will increase the intensity in the spectral line and thus make it weaker relative to the continuum, and vice versa. As the source function largely varies with temperature, it exhibits a gradient through the atmosphere, and deviations from LTE affecting the source function may well be compensated by changes in the line formation depth. The interplay between effects on the formation depth and the source function is thus not obvious.

Figure 2.2 gives a few illustrative examples, computed using the NLTE model of aluminium presented in Paper I (Chapter 3.1). The figure illustrates the relation between the source function and the emergent intensity for two spectral lines of Al I. For each line, the average intensity formation depth has been computed at line centre, and the source function at that point is compared to the emergent intensity. In reality, the contribution function spans a range in depth and the value of the source function at the average formation depth is only an approximation of the emergent intensity. To illustrate this point, the depth where the monochromatic optical depth $\tau_\nu = 0.1$ and 3 are also shown in the figure.

The top panels in the figure illustrate the formation of the Al I 4p–4d transition at 16719 Å, where the source function deviates significantly from the Planck function. This example was calculated for a model of the Sun taken from the (3D) STAGGER grid (Magic et al. 2013a,b). For this line, the NLTE line opacity is smaller than in LTE due to the lower state of the transition being depleted relative to LTE, meaning $\beta_i < 1$. This shifts the formation of the line slightly toward larger reference optical depths. The upper state is more strongly depleted than the lower state, so that $\beta_j/\beta_i < 1$, and consequently the source function is darker than the Planck function, $S_\nu < B_\nu$. Despite the line forming slightly deeper in NLTE, the larger deviation from LTE in the source function results in a significantly stronger line.

The bottom panels of Fig. 2.2 illustrate the formation of the Al I 3962 Å resonance line in the FALC chromospheric model of the Sun (model “C” of

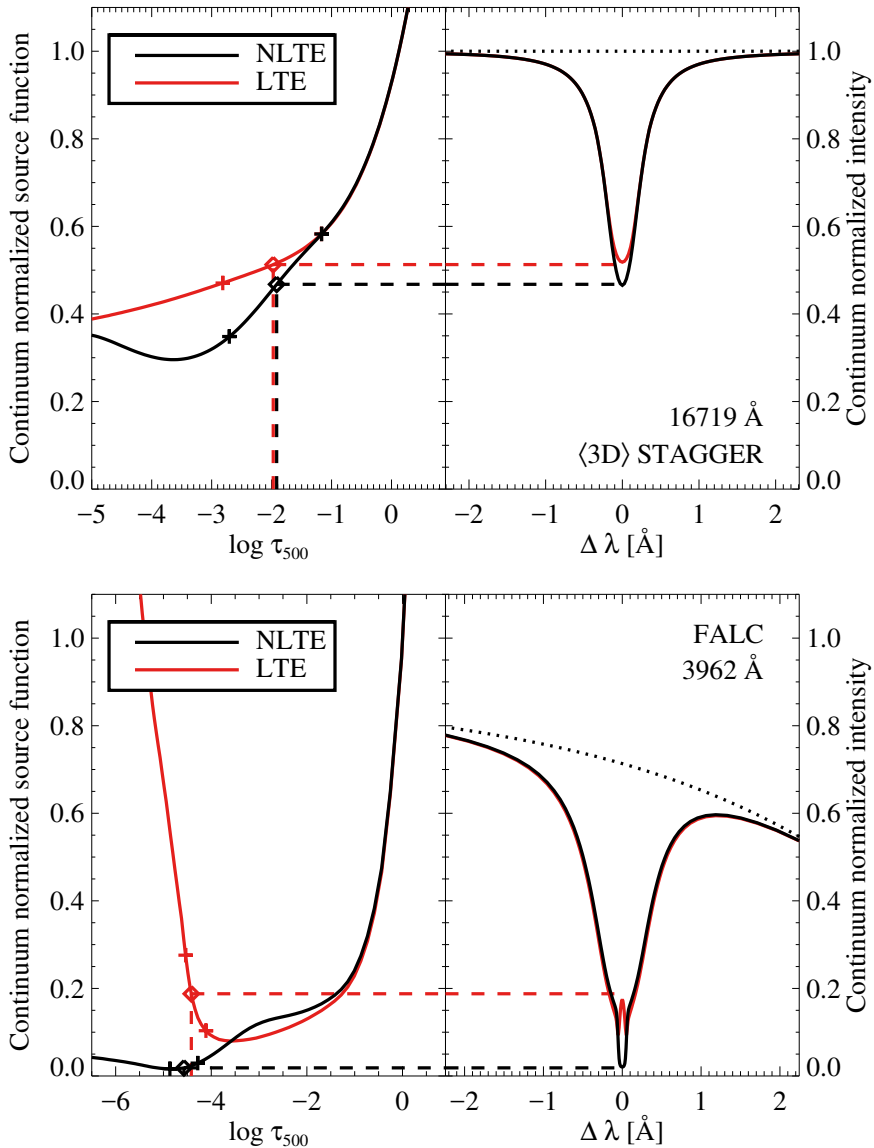


Figure 2.2. Formation of two Al I lines in models of the solar atmosphere, illustrating how the source function S_v (left) relates to the intensity line profile I_v (right) in NLTE (black) and LTE (red). The LTE source function is the Planck function, B_v . All scales have been normalised to the continuum intensity, and the aluminium-free spectrum is shown by the dotted line. The diamonds and dashed lines indicate the average line formation depth, and the source function at that depth. The plus signs denote the points where the monochromatic optical depth $\tau_v = 0.1$ and 3. The upper figure was computed using an averaged hydrodynamical $\langle 3D \rangle$ STAGGER model for the 16719 Å line, and the lower using the chromospheric FALC model for the 3962 Å line where the continuum is depressed by the nearby very strong Ca II H line.

Fontenla et al. 1993). This model exhibits a temperature inversion, reaching a minimum at $\log \tau_{500} \approx -4$ before increasing toward 10 000 K at the top of the chromosphere and 100 000 K in the corona. The Planck function correspondingly increases steeply toward smaller optical depth. Since the line is very strong, the core forms at $\log \tau_{500} \approx -4.5$, well outside the temperature minimum, and the core therefore shows emission in LTE synthesis.

In the NLTE case, the source function is strongly suppressed due to over-recombination and resonance scattering, because the radiation temperature is much lower than the gas temperature in these regions. This results in $\beta_j/\beta_i \ll 1$ and therefore $S_\nu \ll B_\nu$, so that no emission is produced, even though the average formation depth is actually pushed even higher in the atmosphere due to the enhanced line opacity.

Cases where NLTE population reversal causes source function inversion and therefore line emission are known in the literature (Carlsson et al. 1992), and an example is used as a diagnostic for the modelling presented in Chapter 3.1.

2.9 The model atmosphere

In the previous section, two types of model atmospheres were used. The FALC model is a NLTE semi-empirical hydrostatic model of the solar atmosphere, fitted to reproduce the observed UV spectrum. Similar model atmospheres tailored to other stars now exist (Dupree et al. 2016), alongside theoretical NLTE model atmospheres (Hauschildt et al. 1999b,a; Short & Hauschildt 2003). Most studies however use theoretical LTE model atmospheres, such as MARCS (Gustafsson et al. 2008) and ATLAS (Castelli & Kurucz 2004).

All these one-dimensional (1D) models assume *hydrostatic* equilibrium, which is intended to reproduce an average distribution of thermodynamic variables in the stellar atmosphere. Convection is however an inherently time-dependent, three-dimensional (3D) *hydrodynamical* phenomenon. In 1D, time-independent models, convection is thus limited to rudimentary, parametrised descriptions such as mixing-length theory (Böhm-Vitense 1958). The free parameters describing the convective velocity and energy flux are typically calibrated to produce stellar spectra in agreement with observations, or in the case of stellar evolution models to reproduce observed large-scale properties of real stars. While this has proven remarkably useful, the problem is that the calibrations appear to vary with stellar parameters (see Magic et al. 2015).

There are examples in the literature where one or more of the free parameters have been removed. For example, Pasetto et al. (2014) have derived a time-dependent formulation of mixing-length theory from the Bernoulli equation, but the physical quantities turn out to be essentially identical to those from standard mixing-length theory calibrated on the Sun. Additionally, com-

parison to 3D simulations indicate that the physical assumptions underlying their derivations are inappropriate (Arnett et al. 2015).

In contrast to these 1D models, stars like the Sun are not horizontally homogeneous in the atmosphere, but exhibit granulation. This also arises naturally in time-dependent 3D radiation-hydrodynamical simulations, which model convection by solving equations for the conservation of mass, momentum and energy alongside radiative transport. Such calculations have been performed across a wide parameter space, typically using a box-in-a-star setup (see Freytag et al. 2012). In such a setup, the model covers only a small volume on the surface of a star with a sufficient number of convective elements to be representative of the full surface and avoid artificial effects introduced at the boundaries. The top boundary is placed at a height where the gas density is a few orders of magnitude lower than at the optical surface. Since the surface convection zone may cover a significant fraction of the stellar radius – e.g. 30% in the Sun and even more in cooler stars – the bottom of the simulation box usually does not extend to the bottom of the convection zone but is placed a sufficient number of pressure scale heights (~ 5) below the optical surface. In order to conserve mass, outflowing material is replaced by inflowing material of varying pressure but constant entropy, where the latter is the free parameter that determines the effective temperature of the simulation. Along with the surface gravity and chemical composition, these are the only physical free parameters⁴ used for 3D stellar atmospheric models.

An example is shown in Fig. 2.3 comparing a 3D hydrodynamical model of the ultra-metal poor red giant SMSS 0313-6708 to its average, $\langle 3D \rangle$, and a 1D hydrostatic MARCS model. At any given depth, the 3D model exhibits a range of temperatures, which arise because different columns possess different temperature structures. Large differences between the 3D model and the hydrostatic model are seen just below the optical surface, where $\log \tau_{500} \gtrsim 0$. As hot and predominantly ionised buoyant material rises, it quickly radiates away its excess energy due to the strong temperature sensitivity of the H^- opacity, leading to a step-like transition at the edges of granules from temperatures of 10 000 K representative of the interior of granules to 5000 K. Rising material expands adiabatically, causing a decrease in temperature and thus entropy and buoyancy, and returns in the intergranular lanes. Due to the rapid transition from optically thick to thin in the granules, the optical surface appears corrugated as it typically lies higher in these regions than in the intergranular lanes (Stein & Nordlund 1998).

Significant differences are also found in the optically thin outer layers: temperatures are on average significantly lower than in the 1D model as rising material overshooting the convection zone experiences cooling due to adia-

⁴However, additional nuisance parameters are required. These include constants of numerical diffusivity to avoid small-scale oscillations, the damping of standing waves due to the finite geometric extent of the model with periodic horizontal boundaries, and the numerical resolution of the model.

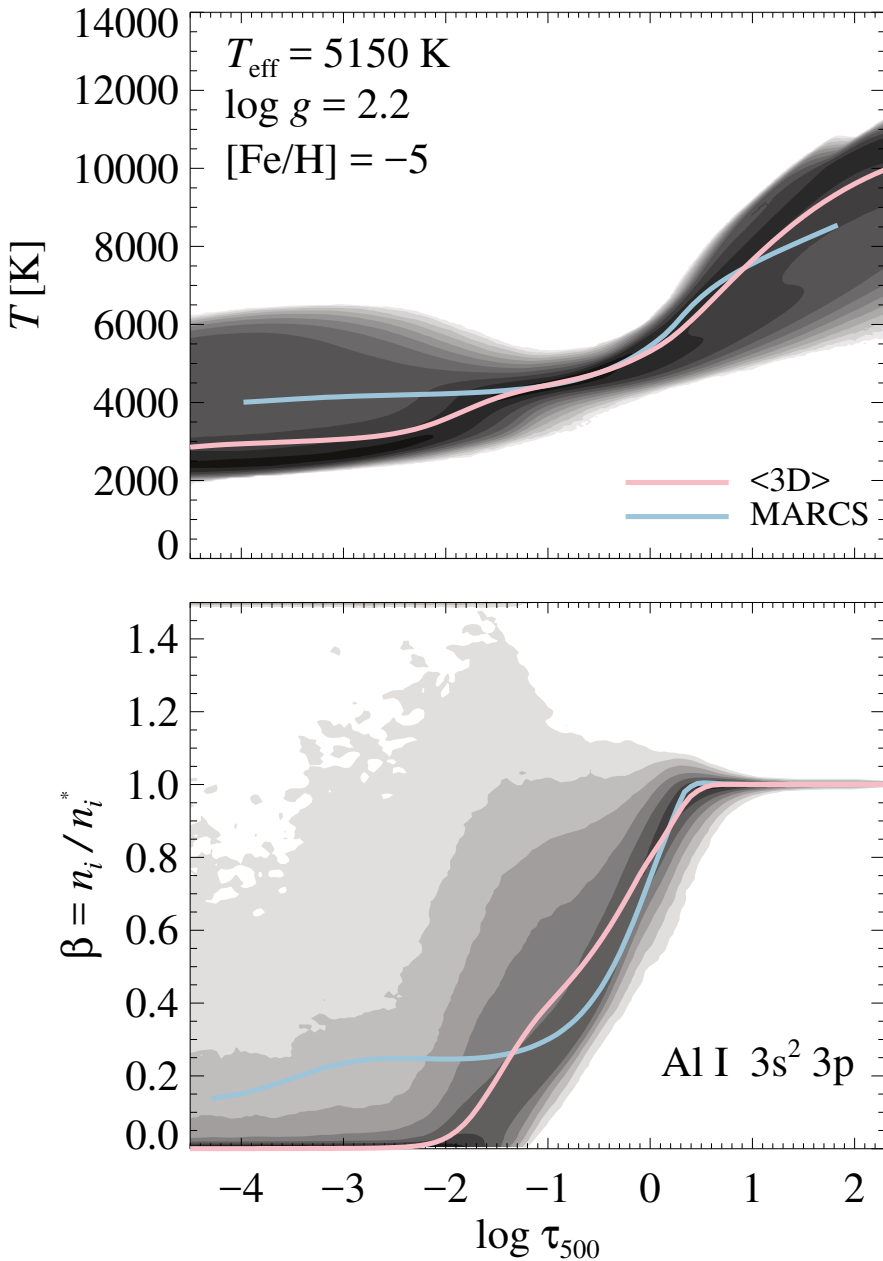


Figure 2.3. Histogram of the temperature distribution (top) and departure coefficient of the Al I ground state (bottom) in a hydrodynamical model of the ultra-metal poor red giant SMSS 0313-6708 (darker colour means higher probability), compared to a one-dimensional MARCS model (blue line) as well as an <3D> model (pink line).

batic expansion. At solar metallicity, these effects are quenched by radiation released near the optical continuum, which is reabsorbed by spectral lines in these layers so that temperatures approach radiative equilibrium. When metal opacities are deficient, adiabatic cooling instead tends to dominate, causing significantly steeper temperature gradients (see Asplund et al. 1999). In terms of line formation, the effect of the stronger temperature gradients in metal-poor models where the line forming regions are significantly colder than in hydrostatic models, is that spectral lines of neutral and molecular species strengthen significantly. This results in lower abundances with 3D–1D abundance corrections as large as -1 dex (e.g., Collet et al. 2007; Dobrovolskas et al. 2013).

The amount of radiative heating depends sensitively on the treatment of coherent scattering. In particular, giant models have sufficiently low density (decreasing absorption opacity) and electron pressure (decreasing collisional rates) that scattering processes become important. Collet et al. (2011) have shown that heating rates computed with a treatment of continuum scattering – meaning $S_\nu = (1 - \epsilon_\nu)J_\nu + \epsilon_\nu B_\nu$ where the destruction probability is $\epsilon_\nu \equiv \alpha_\nu^{\text{abs}} / (\alpha_\nu^{\text{abs}} + \alpha_\nu^{\text{scat}})$ (see Sect. 2.4) – can be well approximated by assuming a Planckian source function ($S_\nu = B_\nu$) and neglecting the contribution to the extinction coefficient due to scattering in optically thin layers. In contrast, treating scattering as true absorption overestimates heating rates in the optically thin layers, leading to significantly higher temperatures closer to radiative equilibrium. Because solar-type models are already near radiative equilibrium, effects of continuum and line scattering are much smaller for them (Hayek et al. 2010).

A second dynamical effect is seen in the uppermost layers where $\log \tau_{500} \approx -3$. As rising gas from adjacent granules expands, compression and supersonic shocks cause significant mechanical heating above the intergranular lanes (Collet et al. 2007; Magic et al. 2013b). These temperature inversions may appear chromosphere-like, but are not caused by magnetic heating and are short-lived. Only a small fraction of the stellar surface is covered at a given time – less than 5% for this particular model.

The lower panel in Fig. 2.3 illustrates the departure coefficients for the ground state of aluminium in the same hydrodynamical and hydrostatic models. The departures from LTE differ between the 1D and $\langle 3D \rangle$ models due to differences in their temperature structures: the warmer layers just beneath the continuum in the 1D model cause stronger overionisation effects in deep optical layers, while the very cool outer layers are strongly overionised in the $\langle 3D \rangle$ model. The 3D model exhibits a wide range of departure coefficients at a given optical depth, ranging from stronger effects of overionisation than in either the 1D or $\langle 3D \rangle$ model, to significant over-recombination in the optically thin layers with departure coefficients even outside the upper range of the plot. The effect of strong over-recombination is typical of regions exhibiting temperature inversions.

2.10 3D radiative transfer

Since 3D models of metal-poor stars are on average colder than 1D models in the optically thin layers and exhibit stronger temperature gradients, spectral lines of temperature-sensitive neutral species are typically strengthened, implying negative 3D–1D abundance corrections (e.g. Asplund & García Pérez 2001). However, line strengths vary significantly across the surface of the model, because the horizontal inhomogeneities cause radiation that propagates along different lines of sight to trace very different conditions. Additionally, because the 3D models contain information about bulk velocities in each volume element, net Doppler shifts arise along any given line of sight, as well as between different lines of sight. Varying Doppler shifts along the line of sight cause a desaturation effect, which in 1D modelling is mimicked by use of microturbulence. Varying Doppler shifts between different lines of sight cause a broadening of the spatially averaged emergent spectrum, which in 1D is represented by macroturbulence (see Asplund et al. 2000). In the shallow layers with temperature inversions, we may expect significant weakening or even emission in the cores of strong lines.

In practice, the emergent spectrum is computed by solving the radiative transfer equation along rays emerging at each grid point at the top of the simulation and propagating along the vertical as well as several inclined directions. With surfaces typically comprised of thousands of grid points ($N_{x,y} \approx N_z \approx 200$), this rapidly leads to large computational cost. To capture the time-dependence of the simulation as it evolves, the spectrum is typically sampled over several snapshots ($N_{\text{snap}} \approx 10$). If the spectrum is computed along $N_\gamma \approx 20$ directions, this implies a total of $N_{x,y}^2 N_{\text{snap}} N_\gamma \sim 10^7$ rays. Compared to 1D radiative transfer where $N_\gamma \approx 10$, the 3D case is of the order 10^6 times more computationally expensive. A spectral wavelength range that in 1D takes only 10 ms to compute, takes of the order 1 hour in 3D. Large spectral intervals, such as the G-band of the CH molecule, may require several months of computations in 3D LTE (Gallagher et al. 2016).

These estimates concern only the calculation of the emergent spectrum. Using a non-local source function with a scattering component or solving the statistical equilibrium adds significantly to the numerical expense. In order to solve the statistical equilibrium, the radiation field must be computed for every relevant frequency ($N_\nu \sim 10^4$) at every volume element in the 3D simulation. This is nowadays performed using short characteristics rays taking into account the 3D radiation field. To speed up calculations, the 3D volume is usually decomposed into sub-volumes which are distributed over different processors – communicating the 3D radiation field between processors may add significant computational overhead. The simplified case where the NLTE solution is computed column-by-column with no horizontal interaction is known as the 1.5D approximation and has proven to be useful (e.g., Pereira & Uitenbroek 2015).

Finally, as the NLTE solution is iterative, this procedure must be repeated a number of times ($N_{\text{it}} \approx 100$) depending mainly on the complexity of the atom. All in all, this leads to calculating of the order $N_{x,y}^2 N_{\gamma} N_{\nu} N_{\text{it}} N_{\text{snap}} \sim 10^{13}$ rays. Such calculations require decades or centuries of CPU time, with calculations for complex atoms and large model atmospheres in the worst cases estimated at hundreds of millennia (e.g. Hauschildt & Baron 2014). Efficiently parallelised codes and large computer clusters are thus required to perform these types of simulations.

Departures from LTE are often larger for realistic 3D atmospheres than in the corresponding 1D models. First, as the temperature structure of metal-poor stars is steeper in 3D models than in 1D, the decoupling between the local thermodynamic variables and the radiation field can be expected to be stronger, leading to stronger NLTE effects. Second, the horizontal inhomogeneities that cause radiation propagating along different lines of sight to form under different conditions, will also lead to varying NLTE effects across the surface of the model (Asplund et al. 2003, 2004). Line formation is a not a linear process, and the average NLTE effect in the 3D model may thus deviate significantly from the NLTE effect in the $\langle 3D \rangle$ model.

As discussed in Paper IV, the 1.5D approximation is not fully sufficient due to the influence of non-vertical radiation. The radiation field at a given point in the model atmosphere depends not only on the temperature structure in that particular vertical column of the 3D model but also on its surroundings (e.g., Stenholm & Stenflo 1977, 1978; Holzreuter & Solanki 2013; Amarsi et al. 2016a; Paper IV). For example, due to radiative losses, the strongest temperature gradients are found just above the optical surface of granules. In the 1.5D approximation, these points are strongly illuminated by the hot region below and the associated large $J_{\nu} - B_{\nu}$ split leads to very strong effects of, e.g., overionisation. However, because the steepest of such gradients typically occur near the edges of granules rather than at their centre, full 3D radiative transfer captures the influence from the cooler immediate surroundings and overionisation is less pronounced.

The opposite behaviour can be found in the temperature inversions occurring above intergranular lanes. In 1.5D, these hot regions are illuminated only by the cool regions below leading to a rather weak mean radiation field, $J_{\nu} < B_{\nu}$, which produces strong overpopulations relative to LTE and thus increased absorption in the line core. In 3D, the intense radiation from the surrounding granules enhances the mean radiation field and the overpopulations are somewhat suppressed. An example of this process can be found in Figs. 3 and 4 of Paper IV, where the NLTE line strength corrections for lines of Ca II and Mg I turn from negative (red colours) to positive (blue) along thin filaments above cool intergranular lanes. While one might think of these peculiar departures from LTE as strange NLTE effects, the opposite case should rather be considered a strange LTE effect. In LTE, the peculiar behaviour comes from the temperature inversion, while in contrast the NLTE level populations fol-

low the radiation field which is smooth and does not exhibit a strong inversion. As such, the situation is analogous to the 1D chromospheric case presented in Sect. 2.8.

2.11 The necessity of 3D NLTE

3D NLTE radiative transfer has only recently become possible and, as mentioned above, the numerical cost involved in this type of modelling is substantial. Therefore, it is of interest to investigate how well simpler methods, e.g., 1D NLTE and 3D LTE, perform in comparison. However, for saturated lines, the comparison is always hampered by the fact that 1D results depend on the adopted microturbulent broadening parameter, v_{mic} .

For lithium, it is well understood that while 3D LTE line formation differs significantly from 1D LTE in warm metal-poor stars (Asplund et al. 1999), the 3D NLTE case is more similar and indeed appears comparable to 1D NLTE for both dwarfs and giants (Asplund et al. 2003; Klevas et al. 2016; Paper IV).

Oxygen has been studied in depth for an extensive grid of model atmospheres by Amarsi et al. (2016a), indicating 3D NLTE–1D NLTE differences on the level of 0.1–0.2 dex, with larger discrepancies (as well as stronger NLTE effects) at lower surface gravity and higher effective temperature. Earlier oxygen studies were limited to the solar spectrum (e.g., Asplund et al. 2004; Pereira et al. 2009a,b; Steffen et al. 2015), where 3D NLTE–1D NLTE differences at disk centre may amount to 0.1 dex.

Because the atoms of sodium and lithium are very similar, their NLTE behaviour is essentially the same when the line strengths are comparable (Lind et al. 2013 and Paper IV) and NLTE and 3D effects essentially cancel. In her analysis of weak lines in the solar disk-centre spectrum, Lind (2010) found small NLTE corrections, with 3D NLTE–1D NLTE abundance differences of the order 0.05 dex, and with similar differences in the predicted centre-to-limb variations.

3D NLTE analyses of magnesium are presented in Paper IV, and have also been performed by Bergemann et al. (2016) for models of metal-poor red giants and a metal-rich dwarf. Both studies indicate 3D NLTE–1D NLTE differences between +0.1 and +0.2 dex with large dependence on the saturation level and the adopted value of v_{mic} .

Aluminium has been studied for the Sun, where NLTE effects are small (Paper I), and for an ultra-metal poor red giant, where NLTE effects are very large (Paper IV). In both cases, 3D NLTE–1D NLTE differences are just 0.01 dex, but larger discrepancies of 0.15 dex are found near the solar limb.

Amarsi & Asplund (2017) analysed weak lines of silicon in the solar disk-centre spectrum, where NLTE effects are very small (0.01 dex). Because the lines form under very similar conditions in 1D and 3D, they find that 3D NLTE–1D NLTE differences are of the order 0.01 dex.

Calcium was studied in 1.5D NLTE by Lind et al. (2013), indicating NLTE corrections as large as +0.8 dex for the Ca I resonance line and -0.4 dex for the infrared Ca II triplet, but they did not compare results to 1D modelling. The Ca II resonance lines were analysed in Paper IV, indicating very large NLTE effects in 3D (+0.5 dex) compared to 1D (+0.15 dex). Consequently, 3D NLTE-1D NLTE differences amounted to 0.3 dex, and removing the difference would require adopting a very small value of v_{mic} and introducing discrepancy between abundances derived from the two resonance lines.

Finally, iron has been studied in 3D NLTE with a simplified model atom (23 atomic levels) for the Sun by Holzreuter & Solanki (2012, 2013, 2015) and later with a comprehensive model atom (> 400 levels) by Lind et al. (2017). While disk-centre line strengths are in good agreement between 3D NLTE and 1D NLTE synthesis, to within 0.05 dex, the centre-to-limb variations may differ by 0.1 dex. The same comprehensive model atom has also been applied to a set of metal-poor standard stars by Amarsi et al. (2016b) and to an ultra-metal poor red giant in Paper IV. NLTE effects are found to be stronger in the 3D models, as large as +1.2 dex, resulting in 3D NLTE-1D NLTE differences of +0.1 dex for the metal-poor stars and +0.2 dex for the ultra-metal poor giant.

In conclusion, 1D NLTE modelling appears to reproduce 3D NLTE abundance results quite well for weak lines when NLTE effects are significant, but discrepancies may be as large as 0.2 dex. Systematic errors are of the order 0.05 dex for the solar flux and disk-centre spectrum. Differences are significantly larger toward the limb, indicating that 1D modelling of centre-to-limb variations is fundamentally unreliable. When NLTE effects are negligible, 3D effects due to either granulation or net differences in the temperature structure appear more important, such that 3D LTE may be more appropriate than 1D NLTE. The opposite case appears to be worse however: because NLTE effects are generally stronger in 3D model atmospheres, 3D LTE synthesis of NLTE sensitive lines will exacerbate errors compared to 1D LTE (see Paper IV and Amarsi et al. 2016b). For saturated lines, it is in principle possible to finetune the v_{mic} parameter in 1D NLTE synthesis to improve the agreement with 3D NLTE results. Additionally, it is not necessarily possible to predict whether NLTE effects will be large *in the 3D model* from analyses of 1D models, as seen in the case of calcium in Paper IV. Thus, while 1D NLTE synthesis largely appears to yield accurate results for weak lines, at least exploratory 3D NLTE work for representative models is necessary to identify the cases where 1D models fail, and the magnitude of the errors.

3. Summary of papers

I give here a brief introduction and summary of the papers presented in this thesis. Details and references are given in each respective paper.

3.1 Paper I

Non-LTE aluminium abundances in late-type stars

Aluminium is of invaluable use for Galactic archaeology. It can be used as a tracer of nucleosynthetic processes during the chemical enrichment of the Galactic bulge, halo, and disk, because the only stable nucleus of aluminium, ^{27}Al , is neutron-rich and its synthesis thus requires a neutron excess. In the metal-free Population III stars exploding as SNe II, the neutron excess is mass dependent, and the abundance of aluminium can therefore be used to determine the initial mass function of the first stars. In the later generations of Population II stars exploding as SNe II, the neutron excess and thus the yield of aluminium is metallicity dependent, while the yield of α -elements is not. In globular clusters, a significant fraction of stars typically exhibit a chemical composition that has been polluted by massive short-lived stars. The magnitude of these anti-correlated abundance variations may be used to determine the nature of the polluting stars, and thereby infer the formation time scales and initial mass of globular clusters.

However, aluminium is known to be severely affected by NLTE effects, which may introduce biases in all these science cases. I therefore present a detailed NLTE study of aluminium, where I use recently available accurate collisional transition data. I perform the very first 3D NLTE analyses of aluminium in the solar spectrum, and find that predictions are in very good agreement with observed centre-to-limb variations of the 7835 Å line as well as an emission line in the mid-infrared at 12.33 μm . The latter is due to a photospheric NLTE population reversal, which is very sensitive to assumptions in the modelling. My abundance analysis of the solar spectrum yields consistent results from different lines ($\sigma = 0.02$ dex), resulting in a solar abundance of $A(\text{Al}) = 6.43 \pm 0.03$ (including systematic errors). This is in exact agreement with the meteoritic abundance, $A(\text{Al}) = 6.43 \pm 0.01$, indicating that the zero-point of the aluminium abundance scale is well determined.

I also analyse a set of metal-rich and metal-poor standard stars with well-known stellar parameters. I use lines in the optical region as well as the

ultraviolet (for metal-poor stars) and the near-infrared, and find consistent abundances from different spectral lines. I have computed extensive grids of abundance corrections, and find that for the commonly used resonance line at 3961 Å, these grow as large as +1 dex in metal-poor stars due to over-ionisation. NLTE effects for subordinate lines are due to a combination of different NLTE mechanisms, and therefore vary rapidly with stellar parameters. These abundance corrections are typically positive for warm stars and negative for cool stars, with more negative corrections at lower metallicity (or lower aluminium abundance). It is thus very important that NLTE corrections are applied, even in studies of similar stars, e.g., in globular clusters.

Finally, I predict the influence of NLTE corrections on previous LTE studies. For example, APOGEE analysed near-infrared spectra of a large sample of 100 000 stars, mainly red giants, inferring a prominent downward slope in $[Al/Fe]$ at low metallicity. Using my NLTE corrections, I find that while abundance corrections vary significantly from star to star at a given metallicity, the average correction is more strongly negative at solar metallicity than at lower metallicity, such that the $[Al/Fe]-[Fe/H]$ trend flattens by at least 0.1 dex. For studies of anti-correlated abundance variations in globular clusters, the abundance corrections vary with metallicity and the evolutionary state of the stars. In addition to significant shifts in the absolute abundance scales, I find that the abundance variations in the most metal-poor clusters may be exaggerated by as much as 0.15 dex. By making my grids of abundance corrections publicly available, it is my hope that they will be used consistently in future studies like these.

3.2 Paper II

Atomic Diffusion and Mixing in Old Stars. III.

Analysis of NGC 6397 Stars under New Constraints

Old, unevolved metal-poor stars in the Galactic halo exhibit a plateau value for their surface abundance of lithium, indicating that its origin is cosmological rather than stellar. However, calculations of Big Bang nucleosynthesis (BBN) in the early Universe yield an abundance higher by a factor 3 than the stellar observations. This so-called cosmological lithium problem has been suggested to be due to the process of atomic diffusion, wherein the surface abundances of lithium and other metals are depleted in unevolved stars due to gravitational settling. As the stars evolve onto the subgiant branch, the deepening surface convection zone restores most metals to the surface, except lithium which has been destroyed by proton-capture reactions in the stellar interior. The initial abundance of lithium must therefore be inferred using stellar evolution models that include the effects of atomic diffusion. These models include a parametrised form of additional mixing which is implemented as a

diffusive process, with diffusion coefficient

$$D(T_0) = 400D_{\text{He}}(T_0) \left[\frac{\rho}{\rho(T_0)} \right]^{-3}, \quad (3.1)$$

where T_0 is a reference temperature (in units of kelvin), D_{He} the atomic diffusion coefficient of helium, and ρ the density. The models are referred to by the shorthand Tx, where $x \equiv \log(T_0)$. Larger values for the reference temperature T_0 result in more efficient mixing, which reaches deeper beneath the convection zone. For reference, proton-capture reactions destroy lithium at a temperature of 2.5×10^6 K, and $\log(2.5 \times 10^6) \approx 6.4$.

Previous observations of stars at varying evolutionary stages in the globular cluster NGC 6397 ($[\text{Fe}/\text{H}] = -2.1$) indicated that surface abundances do indeed evolve, with effects as large as 0.2 dex which vary from element to element. However, these results depend on a number of assumptions, including the adopted effective temperatures of the stars. In particular, it had been suggested that a minor shift of the effective temperatures, in line with new photometric estimates, would essentially remove the observed abundance variations. In this paper, I reanalyse high-resolution spectra of 18 stars, ranging between the main-sequence turnoff point (TOP) and the red giant branch (RGB). In order to increase the signal-to-noise, spectra of stars in the same group are coadded. I determine the abundances of seven elements, taking into account NLTE effects for the five minority species, while the two majority species (Ti II and Fe II) are known to exhibit only very small deviations from LTE. These analyses were performed on three different effective temperature scales, representing different scenarios for how the new photometric data should be interpreted. Regardless of temperature scale, the abundances of Mg and Fe are found to vary with evolutionary state, deviating from the null hypothesis by at least 2σ and 3σ , respectively. The abundances of Mg and Al are known to anti-correlate strongly, but the Al lines are too weak to be detected in these spectra. I find that abundances of Na and Mg also anticorrelate, indicating that the spectroscopic sample contains a mixture of first and second generation stars. By comparing our measured abundances of Na to literature values, I assign first/second generation membership to each star, and find that most of our stars do indeed belong to the second generation. Based on these assignments, I correct the observed abundances of Mg to account for the expected amount of pollution, which acts to flatten the observed trend somewhat.

Finally, the results are compared to stellar evolution models computed for a new estimate of the age of the globular cluster (12 Gyr, based on the white dwarf cooling sequence), which is significantly lower than previous estimates (13.5 Gyr). The lower age is found to yield better agreement with the inferred abundances, especially when the efficiency of additional mixing is low, i.e. T6.0. Adopting the best fitting models, I infer an initial lithium abundance of $A(\text{Li}) = 2.57 \pm 0.1$, which compares well with the BBN predicted value ($A(\text{Li}) = 2.67 \pm 0.07$).

3.3 Paper III

Atomic Diffusion and mixing in old stars VII: Chemical abundance variations in M4

The study of stars in NGC 6397 successfully reproduced the predicted BBN abundance of lithium, but it is not known a priori how the efficiency of additional mixing should vary with metallicity. I therefore investigate abundance variations in the more metal-rich globular cluster M4 ($[\text{Fe}/\text{H}] = -1.1$), in order to make a second, independent, estimate of the effects of atomic diffusion. In this study, I determine the abundances of 14 elements for 86 stars on three different effective temperature scales. NLTE corrections are used for 10 elements, and are found to vary significantly from element to element, as well as with evolutionary state for Li, Al, and Eu.

I find evolutionary abundance variations of 0.1 dex, in very good agreement with predictions from stellar evolutionary models with atomic diffusion where the additional mixing is somewhat more efficient than in NGC 6397, with $\log(T_0) \geq 6.2$. While the predicted evolutionary variations are essentially indistinguishable for most elements between the T6.2 models and those with more efficient mixing, the latter cause lithium to mix to layers where it is partially destroyed on the main sequence. This results in significantly lower predicted surface abundances of lithium, or conversely higher inferred initial abundances. With the conservative choice of using the most efficient mode of mixing that does not significantly deplete lithium on the main sequence, T6.2, I infer an initial lithium abundance of $A(\text{Li}) = 2.59 \pm 0.10$, in excellent agreement with results for NGC 6397, as well as previous results for NGC 6752 ($[\text{Fe}/\text{H}] = -1.6$, $A(\text{Li}) = 2.53 \pm 0.10$ Gruyters et al. 2013, 2014) and M30 ($[\text{Fe}/\text{H}] = -2.3$, $A(\text{Li}) = 2.48 \pm 0.10$, Gruyters et al. 2016).

I find strong, anti-correlated abundance variations among the light elements C, N, O, Mg, Al, and Si, but not Li. This is peculiar, as any nucleosynthetic reaction able to deplete C, O and Mg must have also destroyed any Li that was present. Since the diffusion-corrected abundances of Li exhibit a large star-to-star scatter, uncorrelated with other abundance variations, this implies that Li *production* as well as depletion may have taken place in the polluting objects. While the anticorrelated abundance variations match predictions for fast rotating massive stars of $40 M_{\odot}$, Li production requires contribution from intermediate-mass AGB stars, e.g. via the Cameron-Fowler mechanism. Together, this implies a large initial cluster mass in order to produce sufficient numbers of massive stars, as well as a long formation timescale in order for the intermediate-mass stars to evolve to the AGB stage.

3.4 Paper IV

3D NLTE analysis of the most iron-deficient star, SMSS0313-6708

The chemical compositions of the most metal-poor stars are generally consistent with the predicted yields of low-energy core-collapse supernovae whose progenitors were massive ($20\text{--}60 M_{\odot}$) Population III stars. This is surprising, since cosmological simulations predict that the first stars were typically very massive (up to $300 M_{\odot}$). Such stars would have exploded in pair-instability supernovae, producing large quantities of metals with a very different chemical composition from what has actually been observed. However, comparisons to the predicted chemical yields from core-collapse supernovae are hampered by the fact that the explosion mechanism is not well understood, and is parametrised in the models. In order to accurately determine the properties of the supernova explosion and the progenitor star, the chemical composition of the star must be accurately determined. In particular, NLTE effects are known to become more severe at lower metallicity, and the interplay between the steeper temperature structures of 3D model atmospheres (compared to 1D models) and the NLTE effects is largely unknown.

I therefore perform a 3D NLTE abundance analysis of the most iron-poor star known, the red giant SMSS0313-6708. This is the first time such modelling is used to determine the chemical composition of any star other than the Sun. The remarkable spectrum of this star only contains measurable atomic lines of hydrogen, lithium, magnesium, and calcium, as well as lines of the CH and OH molecules. Only upper limits can be determined for other elements, including every odd-Z element heavier than lithium and indeed every element heavier than calcium, including iron.

My 3D NLTE analysis indicates higher abundances compared to 1D LTE, by 0.8 dex for iron, and by 0.5 dex for magnesium, aluminium, and calcium, while differences are small (< 0.03 dex) for lithium and sodium. The new higher abundances and upper limits are in very good agreement with predictions from supernova models. I find that progenitor stars in a wide range of masses ($10\text{--}60 M_{\odot}$) match observations well due to a degeneracy between progenitor mass and supernova explosion energy. At any given mass, the explosion energy is however well constrained and never exceeds 2.2×10^{51} erg. Such low energies are not sufficient to eject material near the core of the progenitor star from the gravitational well, and are characteristic of the type of faint “fall-back” supernovae expected from massive Population III stars. I can strongly reject higher explosion energies, including the pair-instability supernovae expected to result from very massive stars.

4. Conclusions and outlook

In this thesis, I have presented a few of the central science cases of Galactic archaeology with metal-poor stars. My focus has been on the challenges and potential pitfalls, and how we may deal with them. In particular, the assumption of LTE level populations and the use of 1D model atmospheres for the calculation of synthetic spectra may seriously bias how we interpret observations. By performing detailed NLTE and 3D NLTE calculations, I have shown that these biases may be as large as 1 dex for very important elements such as iron and aluminium. The systematic errors are not limited to Population II stars, but affect stars at solar metallicity too, in particular when the spectral lines are saturated.

4.1 Atomic diffusion

I have also shown that a group of non-standard stellar evolutionary effects, known collectively as atomic diffusion, affect the chemical composition of unevolved metal-poor stars by as much as 0.2 dex at very low metallicity ($[\text{Fe}/\text{H}] = -2.1$). These effects vary from element to element, with metallicity, and with the evolutionary state of the star. They are known to be small at high metallicity, e.g., ≤ 0.05 dex in the solar-metallicity open cluster M67 (Önehag et al. 2014), and as large as 0.3 dex in the $[\text{Fe}/\text{H}] = -2.3$ globular cluster M30 (Gruyters et al. 2016).

The behaviour at even lower metallicity is not yet understood and there are no Galactic globular clusters that can be used to investigate the size of the effect in this regime. However, assuming that all old and metal-poor field stars in the halo were born with the same primordial lithium abundance, trends with metallicity and mass may be enlightening. The uniform plateau of surface lithium abundances found in unevolved metal-poor stars with metallicities in the range between $[\text{Fe}/\text{H}] = -1$ and -2.5 , is known not to extend to lower metallicity (Sbordone et al. 2010). The mass-dependency of this additional depletion of lithium is reproduced at extremely low metallicity, $[\text{Fe}/\text{H}] = -2.5$ to -3.5 , by stellar evolution models taking into account atomic diffusion if efficient additional mixing is used (Meléndez et al. 2010a). This is the complete opposite behaviour to expectations based on extrapolating our findings from globular clusters at $[\text{Fe}/\text{H}] = -1.1$ to -2.3 , to lower metallicity.

Calculations at extremely low metallicity that neglect additional mixing predict exceedingly large over-abundances as large as 1 dex for turnoff stars

(Richard et al. 2002a). It is therefore of utmost importance that more studies of atomic diffusion focus on extremely low metallicity. First steps in this direction have already been taken with the studies of lithium in field stars mentioned above as well as studies of extremely metal-poor spectroscopic binaries (Norris et al. 2000; González Hernández et al. 2008; Aoki et al. 2012). Unfortunately, the large abundance measurement uncertainties do not allow any firm conclusions on whether diffusion effects have been detected in these stars, for elements other than lithium. If stars such as these are used for further study of the effects of atomic diffusion, it is important that abundances are derived using the most accurate methods possible, i.e., 3D NLTE synthesis.

4.2 Beyond 3D NLTE

Results presented in Paper I and Paper IV of this thesis, as well as those of Amarsi et al. (2016a,b), and Lind et al. (2017), convincingly show that our predictions based on 3D NLTE synthesis do apply to real stars, and that differences compared to 1D LTE, 1D NLTE, and 3D LTE synthesis may be very large. But even with state-of-the-art 3D NLTE radiative transfer, there are shortcomings and approximations whose impact must be considered.

First, concerning the NLTE modelling itself, the accuracy and completeness of collisional and radiative transition rates may significantly affect results (see the review by Barklem 2016a). In particular, the Drawin formula does not describe the physics of hydrogen collisions (Barklem et al. 2011), and astrophysical calibration factors may vary by orders of magnitude between different authors and elements (Bergemann & Nordlander 2014). Despite the recent progress with calculating quantum mechanical cross-sections of hydrogen collisions, only a handful of astrophysically important elements; Li, O, Na, Mg, Al, Si, Ca, and Fe, may today be considered free from strongly influential free parameters in this respect. Furthermore, incomplete term diagrams may result in insufficient collisional coupling between highly excited states and the continuum, thus exaggerating deviations from LTE (e.g., Gehren et al. 2001a,b; Korn et al. 2003; Mashonkina et al. 2011). As discussed by Gehren et al. (2001a), this is likely the reason why the analysis by Gratton et al. (1999) required very efficient hydrogen collisions in order to thermally couple high-excitation states of Fe I to the Fe II continuum, resulting in essentially LTE populations everywhere. While theoretical photoionisation data often reproduce observed threshold cross-sections well, uncertainties in the locations of narrow resonances are typically several times larger than their widths (Bautista et al. 1998).

NLTE analyses of late-type stars typically adopt the trace element approximation, and this includes the work presented in this thesis. This approximation is based on the assumption that effects on the element under study do not affect the atmospheric structure, and that different elements may be analysed

independently using pre-computed tabulations of background line opacities in LTE. This assumption may be unsuitable in cases where important transitions of different elements overlap and are affected by departures from LTE. For example, Shi et al. (2008) note that the strongest bound-bound transitions of Si I are located at $\lambda < 2000 \text{ \AA}$, where they are suppressed by the strong bound-free edge of the Al I ground state, leading to near-LTE populations in all states of Si I out to small optical depths in the solar photosphere. While my results show that Al I is not strongly overionised in the relevant layers of the solar photosphere, it should be verified if Si I can safely be analysed in the trace element approximation, or if NLTE opacities of Al need to be considered.

Second, 3D models in common use today are constructed under the assumption of LTE radiation transport, and without magnetic fields. 1D NLTE model atmospheres deviate from the LTE radiative equilibrium in their outermost layers due to the overionisation of light and iron-peak elements (Short & Hauschildt 2005, 2006), but it is unknown what the corresponding effects would be in 3D. Large-scale magneto-hydrodynamical (MHD) simulations utilising NLTE ionisation of hydrogen exist for the Sun (e.g., Freytag et al. 2012; Carlsson et al. 2016), but not yet for any other star. In models where a strong mean magnetic field of 200 G is used, the average temperatures in optically thin layers may be higher by up to 100 K due to local effects in regions of large magnetic flux concentrations. Within such regions, magnetic pressure replaces a fraction of the gas pressure, leading to lower densities and thus lower opacities. In LTE, the influence on abundances is typically small (< 0.05 dex), but effects may be as large as $+0.1$ dex for highly temperature sensitive low-excitation lines (Pereira et al. 2013) with relatively small dependence on the magnetic sensitivity (Landé factor) of the lines in the optical region (Fabbian et al. 2010, 2012). However, the magnetic field must be concentrated and coherent for effects to be this large, as the small-scale magnetic fields expected to arise from local dynamo actions have been found to have negligible effects on abundances (≤ 0.01 dex, Moore et al. 2015).

Other potential problems include the neglect of sphericity effects. When the model domain covers a significant fraction of the stellar surface, as may be the case in giant stars, the curvature of the stellar surface may become important essentially because the top of the atmosphere has larger surface area than the bottom, thus diluting vertical fluxes. These effects have been investigated in detail for 1D models in radiative equilibrium, where effects of sphericity generally lead to lower temperatures in the outer atmospheric layers (e.g. Jørgensen et al. 1992; Plez et al. 1992; Hauschildt et al. 1999b; Short & Hauschildt 2003; Gustafsson et al. 2008) in addition to smaller direct effects on the line formation (Heiter & Eriksson 2006). In 3D hydrodynamical simulations of metal-poor stars, the outer layers of the atmosphere are typically not in radiative equilibrium, and the interplay between diluted convective and radiative fluxes due to geometric effects has not yet been explored.

The model atmospheres used in abundance analyses typically lack chromospheres, despite ample evidence that these are present also in metal-poor stars (e.g. Peterson & Schrijver 2001; Takeda & Takada-Hidai 2011). Although the spectral lines commonly used form entirely in the photosphere, radiation from the chromosphere may affect photospheric NLTE level populations (e.g. Przybilla & Butler 2004). The semi-empirical model atmospheres constructed for metal-poor giants by Dupree et al. (2016) yield significantly lower abundances than the corresponding non-chromospheric models. However, also the temperature stratification of photospheric layers is modified in their models and the relative influence on abundance measurements from direct and indirect effects of the chromosphere is not clear.

Finally, only a very limited number of studies have considered NLTE effects on the statistical and molecular equilibrium of molecules due to their formidable complexity. This is potentially of great concern for Galactic Archaeology, because molecular bands are often the only useful diagnostic of C, N, and O abundances in extremely metal-poor stars. A typical heteronuclear diatomic molecule like CO or OH has several relevant electronic states, each of which may be excited vibrationally as well as rotationally, resulting in many thousands of energy levels with tens of thousands of important radiative transitions. Due to their close energy spacing, rotational as well as vibrational levels may be efficiently collisionally coupled and thus exhibit relative LTE populations where every such level has the same departure coefficient β_i . On the other hand, electronic excitation of molecules requires more energetic impact particles, and the relative populations of different electronic states may deviate strongly from LTE. While NLTE modelling of molecules suffers from the same problems as listed above for atoms, in particular uncertainties in radiative and collisional transition rates, the large number of close-lying energy levels and radiative transitions also leads to additional numerical difficulties.

The CO molecule has been modelled by Ayres & Wiedemann (1989) and Uitenbroek (2000), who concluded that the vibration-rotationally excited states are indeed in collisional equilibrium and that NLTE effects are therefore small for vibrational-rotational lines. However, they found that the collisional formation of the CO molecule is relatively slow compared to solar dynamical timescales, and Asensio Ramos et al. (2003) have since shown that time-dependent molecular formation may be important in regions of the solar photosphere that evolve rapidly, so that non-equilibrium populations arise due to dynamical rather than radiative effects. The statistical equilibrium of the OH molecule in metal-poor atmospheres has been studied by Asplund & García Pérez (2001), using a two-level atom that represents electron excitation for a single UV transition. They concluded that while the line opacity follows LTE, line scattering causes a significant brightening of the line source function thus weakening the line, as was predicted by Hinkle & Lambert (1975). Finally, Lambert et al. (2013, 2015) have studied NLTE line formation of the H₂O molecule in the cool low-density atmospheres of red supergiants. Prelim-

inary results from their detailed treatment of the very large set of close-lying energy levels (~ 1000) and radiative transitions ($\sim 10\,000$), indicated large deviations from LTE among rotational levels in the ground vibrational state, as well as large deviations for the high-excitation vibrational states where rotational levels were found to be in collisional equilibrium. NLTE effects thus vary from band to band, and indeed between the low- and high-rotational lines in the same band.

Molecular line analyses of metal-poor stars in LTE are known to yield very large differences between 3D and 1D models (e.g., Collet et al. 2006; Behara et al. 2010; Bessell et al. 2015; Gallagher et al. 2016; Prakashavičius et al. 2016). It is important to ensure that the usually significantly lower abundances resulting from 3D models are indeed more accurate and not strongly biased by the LTE assumption, or our conclusions on the chemical enrichment of the Galaxy may become severely misguided.

5. Contributions to the included papers

Paper I

Nordlander, T. & Lind, K. (2017)

Non-LTE aluminium abundances in late-type stars

Astronomy & Astrophysics, submitted Jan. 2017

The project was suggested by and then defined in collaboration with the coauthor, Karin Lind. I built the atomic model using literature data, and performed tests on its completeness and validity. I compiled observational data from the literature, and wrote and executed the pipelines for abundance analysis and comparison to the solar intensity spectrum. I set up and performed all LTE and NLTE calculations presented in the paper. I led the writing of all sections of the paper, with input from the coauthor.

Paper II

Nordlander, T., Korn, A. J., Richard, O., & Lind, K. (2012)

Atomic Diffusion and Mixing in Old Stars. III.

Analysis of NGC 6397 Stars under New Constraints

The Astrophysical Journal, 753, 48

The project scope was suggested by and then defined together with Andreas Korn. I determined the new effective temperature scales, performed the abundance analysis, compiled 3D and NLTE effects from literature and collaborators, and designed the approach to remove effects of pollution on the abundance trends. I led the writing of all sections of the paper, with strong input from the coauthors.

Paper III

Nordlander, T., Gruyters, P., Korn, A. J., & Richard, O. (2017)

Atomic Diffusion and mixing in old stars VII:

Chemical abundance variations in M4

To be submitted to *Astronomy & Astrophysics*

The project was suggested by Andreas Korn, and the analysis was carried out in strong collaboration with Pieter Gruyters. Together, we defined the methodology for the photometric analysis and the spectroscopic approach, including the selection of lines. I wrote and executed the photometric dereddening tool, the pipelines for spectroscopic stellar parameter and abundance analysis, and produced all figures for the paper. Pieter Gruyters led the writing of the paper which was initially submitted to *Astronomy & Astrophysics* in 2015 with him as lead author. I contributed the bulk of the analysis section, and coauthored the sections on the observations, results and discussion. After receiving a very lengthy referee report, I took over the lead of the project, and spent considerable time improving the analysis. This has led to minor changes throughout the paper, which will be resubmitted to *Astronomy & Astrophysics* early this year, now with myself as the lead author.

Paper IV

Nordlander, T., Amarsi, A. M., Lind, K., Asplund, M., Barklem, P. S., Casey, A. R., Collet, R., & Leenaarts, J. (2017)
3D NLTE analysis of the most iron-deficient star, SMSS0313-6708
Astronomy & Astrophysics, 597, A6

The project was suggested by Martin Asplund, and the research was initiated during a visit to the stellar spectroscopy group at Mount Stromlo Observatory in Canberra, Australia. I modified the comprehensive model atoms for use with the Multi3D code with help from Karin Lind, who compiled the model atoms except for Al. I executed the test and production runs, with extensive guidance by Anish Amarsi. I designed and executed the abundance analysis and the comparison to supernova model yields. I led the writing of all sections of the paper, with input from all coauthors.

6. Svensk sammanfattning

Vår bild av universums tillkomst och utveckling är grundad i observationer. Observationer av den kosmiska bakgrundstrålningen och universums storskaliga struktur är konsistenta med ett ursprung i Big Bang, och indikerar att universum idag domineras av mörk materia och mörk energi, snarare än av vanlig materia. De första grundämnena, väte, helium och små mängder av litium, tillkom ungefär tre minuter efter Big Bang. I princip alla tyngre grundämnen, som inom astronomin kallas för metaller, har bildats vid kärnreaktioner i stjärnor och spritts av stjärnvindar eller supernovor. Även om till exempel jordklotet huvudsakligen består av metaller, som alltså bildats i stjärnor, så utgörs atmosfären hos solen och liknande stjärnor till överväldigande del av vätgas (73 % av massan) och helium (25 %), och de resterande 2 % av syre, kol och andra så kallade metaller.

En stjärnas öde bestäms huvudsakligen av dess massa: stjärnor med mindre massa än solen har livslängder som mäts i tiotals miljarder år. Eftersom deras livslängd är jämförbar med eller längre än universums nuvarande ålder, kan lågmassiva stjärnor användas till att spåra galaxens egenskaper bakåt i tiden, i en process vi kallar galaktisk arkeologi.

I solens kärna pågår kärnreaktioner som omvandlar väte till helium samtidigt som energi frigörs, och dessa processer kommer att pågå under huvuddelen av solens liv, vad som kallas huvudserien. När vätet tar slut så kollapsar kärnan så att temperatur och tryck ökar, samtidigt som de yttre lagren sväller upp och kallnar av. Denna utvecklingsfas kallas röda jättegrenen och fortsätter till dess att omvandlingen av helium till kol och syre påbörjas i kärnan. När de yttersta lagren blir kallare så förstärks de hydrodynamiska konvektionsprocesserna så att de når djupare och djupare, och till och med för upp förbränningsrester från kärnreaktioner till stjärnans yta. Under jättestjärnans vidare utveckling uppstår kraftiga vindar som kastar av stjärnans yttre lager och exponerar dess heta kärna, som vi kallar en vit dvärg. Eftersom jättestjärnans yttre lager innehöll förbränningsrester, så är detta ett exempel på de processer som berikar galaxen med vissa tyngre grundämnen samt stoftpartiklar.

De flesta stjärnor föds i grupper om två eller fler. I binära stjärnsystem där den ena stjärnan är outvecklad (befinner sig på huvudserien) när den andra har utvecklats till en vit dvärg, kan det hända att stjärnorna kretsar tillräckligt nära varandra att massa spillas över från huvudserie-stjärnan till den vita dvärgen. Ifall den vita dvärgens massa ökar tillräckligt, kan kärnförbränning av kol inledas. Detta är en våldsamt och instabil process som leder till en supernova av typ Ia. Dessa producerar stora mängder av bland annat järn som kastas ut i

galaxen. Trots att dessa händelser är relativt ovanliga så har huvuddelen av allt järn i solsystemet producerats på detta vis.

Massiva stjärnor kan efter omvandlingen av väte till helium och vidare till kol och syre, starta ytterligare kärnreaktioner. Dessa omvandlar kol och syre till neon och vidare till ännu tyngre ämnen, och samma process pågår även i lägre tempo i skal som omger kärnan. Efter att järn har bildats kan ingen mer energi utvinnas, utan stjärnans kärna kollapsar igen och omvandlas under högt tryck till att enbart bestå av neutroner. Eftersom en kärna som består helt av neutroner är mycket styv, studsar de infallande yttre lagren mot denna så att chockvågor uppstår, vilket tillsammans med strålning av neutriner från den heta kärnan orsakar en supernova av typ II. Dessa producerar stora mängder av exempelvis syre, och har därmed bildat huvuddelen av allt vatten i universum.

De stjärnor som har riktigt stor massa har samtidigt högst tryck och temperatur i kärnan, och har därför snabbast förbränningstakt. Eftersom detta innebär att de blir kortlivade, så bör supernovor av typ II ha exploderat tidigt under galaxens utveckling, strax efter att de första massiva stjärnorna bildades. Lågmassiva stjärnor är mer långlivade, så först miljarder år senare sker supernovor av typ Ia, och detta visar sig vara synligt i stjärnors kemiska sammansättning. De äldsta, mest metallfattiga stjärnornas kemiska sammansättning liknar vad som förväntas produceras i supernovor av typ II. Endast yngre stjärnor såsom solen innehåller även material från supernovor av typ Ia.

Stjärnors kemiska sammansättning bestäms spektroskopiskt, genom att vi jämför ett observerat spektrum med teoretiska beräkningar, och anpassar fysikaliska parametrar i modellen till dess att de matchar observationerna. Varje atom och varje molekyl har ett unikt fingeravtryck i form av våglängden hos dess spektrallinjer. Energitillstånden i atomer och molekyler är kvantiserade, har fixa värden, och därför är skillnaderna i energier också kvantiserade. För att en foton ska kunna absorberas av en atom eller molekyl, så krävs det att energin hos fotonen motsvarar skillnaden mellan två energinivåer. Fotoner med precis rätt våglängd har högre sannolikhet att absorberas av gasen jämfört med fotoner av närliggande våglängd, vilket visar sig i form av en spektrallinje. Ju större förekomst av en viss atom, desto starkare blir dess spektrallinjer. En stjärnas kemiska sammansättning kan därför bestämmas bara genom att analysera dess spektrum.

Men, de teoretiska beräkningarna av en stjärnas spektrum är komplicerade och man tvingas därför göra flera förenklingar. Vissa av dessa antaganden har visat sig vara olämpliga, och resultaten blir därför missvisande särskilt för metallfattiga stjärnor och för jättestjärnor. De fel detta leder till kan vara så stora som en storleksordning, vilket i praktiken gör att den galaktiska arkeologin ibland skjuter i blindo. Även om man inte alltid kan ta hänsyn till dessa effekter i analysen av varje stjärna, så måste vi åtminstone kunna bestämma hur pass stora de är i ett par typiska fall. I denna avhandling presenterar jag analyser av stjärnor där beräkningarna utförs utan vissa av dessa förenklade antaganden.

Det första antagande som brukar göras är att fördelningen över atomernas olika excitations- och jonisations-tillstånd i stjärnatmosfärer befinner sig i jämvikt enligt Boltzmanns och Sahas ekvationer. Implicit antas då att atomerna kolliderar mer frekvent med andra gaspartiklar än de interagerar med fotoner, i vad man kan kalla för kollisionell jämvikt. När man tar hänsyn till hur fotoner propagerar och interagerar med atomer, så påverkas en stjärnas beräknade spektrum. Denna typ av modellering kallas icke-lokal termodynamisk jämvikt (på engelska: non-local thermodynamic equilibrium, NLTE) och kräver att man kan uppskatta sannolikheten för olika atomära processer väl.

Det andra antagandet gäller att en stjärnas atmosfär, dvs det tunna yttersta lagret som släpper ifrån sig strålning, befinner sig nära hydrodynamisk jämvikt och att variationer i temperatur och densitet i horisontell utsträckning över ytan inte påverkar spektrallinjebildningen. Ifall detta stämmer, så kan man approximera stjärnatmosfärer med endimensionella modeller, som beskrivs endast som funktion av djup. I själva verket vet vi att solens yta uppvisar vad som kallas granulering, där konvektionsprocesser leder till att bubblor av hetare material stiger mot ytan, kyls ned, och strömmar ned igen. Det visar sig att det varierande hastighetsfältet och skillnaderna i temperatur och tryck som uppstår över ytan är nödvändiga att modellera enligt hydrodynamikens lagar (statiska modeller tvingas förenkla och parameterisera konvektion). Effekten av granulering visas på omslaget till denna avhandling, baserat på NLTE-beräkningar för en 3D-modell av en metallfattig röd jättstjärna (se nedan).

Just kombinationen av NLTE-effekter och granulering i 3D-modeller har visat sig vara viktig. Tyvärr är sådana beräkningar mycket omfattande, i storleksordningen miljarder gånger mer krävande än när man använder endimensionella modeller och antar kollisionell jämvikt. Det betyder att de kan ta tiotals år av processortid, vilket i praktiken innebär ungefär en vecka vid parallellisering över hundratals processorer för att beräkna spektrumet av en enda atom för en enda stjärna.

Jag undersöker i denna avhandling vikten av dessa effekter, först i en teoretisk studie av aluminium. Aluminium är ett viktigt grundämne som kan användas vid studier av galaxens tidiga utveckling, övergången från supernovor av typ II till typ Ia, utvecklingen av massiva stjärnhopar, och mer. Denna studie inkluderar 3D-NLTE-beräkningar för solspektrumet, vilka visar god överensstämmelse med observationer. Skillnaderna mot traditionell modellering är däremot inte särskilt stora när det gäller solen – de förenklade antagandena är alltså acceptabla för sol-lik stjärnor. Däremot blir effekterna mycket stora vid låg metallicitet samt i metallrika jättstjärnor.

Jag presenterar även två studier av stjärnor i metallfattiga stjärnhopar. Dessa studier fokuserar på att testa den galaktiska arkeologins mest fundamentala antagande: att den kemiska sammansättningen av stjärnors atmosfärer inte förändras över tid. Jag påvisar att mikroskopiska processer som kallas atomisk diffusion leder till att tyngre grundämnena sipprar ned från de synliga ytlagren och djupare ned i stjärnan. Om detta inte tas hänsyn till, blir analyser av dessa

stjärnor därför missvisande oavsett hur avancerad modellering av spektra som används. För att bestämma hur pass stora dessa effekter är, analyserade vi i två artiklar metallfattiga stjärnor i olika stadium av sin utveckling, mellan huvudserien och röd jätte. Vi fann att stjärnor i huvudserien har något annorlunda kemisk sammansättning än röda jättar. Detta eftersom de flesta ämnen som sipprat ned har kommit upp till ytan igen hos jättestjärnorna genom djupa konvektionsprocesser. De skillnader vi fann i kemisk sammansättning matchar modeller väl, vilket indikerar att vi kan förutspå hur den kemiska sammansättningen hos en given stjärna som befinner sig i huvudserien har påverkats, och i princip kan vi korrigera detta. Men, vi vet ännu inte vad som händer vid mycket låga metallhalter. Vi vet i grova drag att den kemiska sammansättningen hos mycket metallfattiga stjärnor i huvudserien inte exakt reflekterar den som stjärnan, och därför galaxen, hade vid stjärnans födelse, men vi kan inte förutsäga hur stor effekten är. Detta är ett problem för galaktisk arkeologi, och bör undersökas igen i framtiden.

Slutligen presenterar jag en 3D-NLTE-studie av en röd jätte, som är en av de mest metallfattiga stjärnor som vi känner till. Den är så metallfattig att inte ens linjer av järn, som normalt är mycket framträdande i stjärnors spektra, syns. Med hjälp av 3D-NLTE-beräkningar, där ett exempel visas på omslaget till denna avhandling, bestämde vi stjärnans kemiska sammansättning. Vi fann att antagandet om kollisionell jämvikt ger kraftigt missvisande resultat och att i praktiken så kommer 3D-NLTE-beräkningar att behöva utföras för varje sådan stjärna som hittas. Stjärnans kemiska sammansättning indikerar att den anrikats med materia från en enda supernova, vilket betyder att stjärnan måste ha bildats mycket tidigt i galaxens historia. Den kemiska sammansättningen indikerar att denna supernova skiljer sig från vanliga supernovor genom att den varit ovanligt ljussvag. Den stjärna som exploderat var dessutom helt fri från metaller och måste alltså ha varit en av de allra första stjärnor som föddes i vår galax, innan andra supernovor hunnit äga rum. Modellerna visar vidare att den stjärna som föregick supernovan bör ha varit mellan tio och sextio gånger tyngre än solen. Resultatet är förvånande, då man tidigare tänkt sig att de allra första stjärnorna bör ha varit mycket massiva, med massor kanske hundratals gånger större än solens.

Dessa är några exempel på den information som kan utrönas om universums och vår galax tidiga utveckling utifrån observationer av lågmassiva stjärnor. Mina resultat visar att det är mycket viktigt att ta hänsyn till NLTE-effekter i dessa studier, och särskilt för de mest metallfattiga stjärnorna.

7. Acknowledgements

I extend my deepest thanks to Andreas Korn, who has supervised not only the work in this thesis, but also my bachelor's thesis. You have provided support and encouragement from the very beginning, which convinced me that research in astronomy was my calling. Your scientific advice and guidance has been invaluable.

I am grateful to Karin Lind for stepping in as my de facto main supervisor halfway through my doctoral studies, which allowed my research to broaden toward something new and even more exciting. Your ability to give helpful answers to the most misguided questions is greatly appreciated!

To Ulrike Heiter, for supporting my Gaia-related work, and providing guidance throughout my graduate as well as undergraduate studies.

I would also like to thank my “bonus supervisors” who have provided insights and advise for various projects. Hans Rickman, for urging that we continue and finish our project on the origin of the Oort cloud (which was not part of this thesis). I am grateful for your support, your conviction that our work could be perfected, your will to see to it that it was, and for you amazing analytical ability. Bengt Gustafsson, for your commentary and enthusiasm on every project I have been involved in. Science should be fun, and you make it fun! Nikolai Piskunov, for your patience, guidance, and support. During my master's thesis, the SME development efforts, and my never ending stream of confused questions. Paul Barklem, for guiding me toward a rudimentary understanding of atomic physics, and for advice on science and a scientific career. Kjell Eriksson, for your deep knowledge of all things radiative, and your helpful suggestions on much of my scientific work. Martin Asplund, for suggesting the project and inviting me to Canberra for the scientific collaboration which amounted to Paper IV (and the cover of A&A as well as a science highlight!). Thank you for your endless enthusiasm!

I extend thanks to my close collaborators, who have contributed to my scientific development as well as to this very thesis. To Pieter Gruyters, for your contribution to our research, your strong opinions – scientifically and otherwise – and for your friendship. For making me understand the beauty of Belgian beer, and for accepting my hate of Thor (the Marvel character, not the god). To Anish Amarsi, for your patient help and scientific ability, without which Paper IV would have taken twice as long and turned out half as good.

I also wish to thank my family, friends, and colleagues – most of you unnamed but none forgotten. Special thanks to Sofie, for being the best office mate ever, and a great friend. For encouraging over-indulgence of tiramisu,

mountain biking, and deep-fri(e)days. To Lisa, my oldest astronomy-friend. Your amazing positivity and sincere goodness is an inspiration! To Alexis, especially for your help producing the cover of this thesis. To Sara, for tolerating my terrible jokes and for at times being even worse (better?), and to Jonathan and Naum for *always* being worse (better?). To Christian, for your absurdly hilarious stories (and to Linnéa for helping us figure out a few more). To Samuel, for being the social engine the astronomy corridor needs. To James, for your help with Selene and Balder. And for being awesome.

Finally, to Jessica. Without your insistence, I would have likely given up my studies and never moved to Uppsala. You help me improve, and to want to improve. You make it all worthwhile.

References

- Abadi, M. G., Navarro, J. F., Steinmetz, M., & Eke, V. R. 2003, *The Astrophysical Journal*, 597, 21
- Abel, T., Bryan, G. L., & Norman, M. L. 2002, *Science*, 295, 93
- Amarsi, A. M. & Asplund, M. 2017, *Monthly Notices of the Royal Astronomical Society*, 464, 264
- Amarsi, A. M., Asplund, M., Collet, R., & Leenaarts, J. 2016a, *Monthly Notices of the Royal Astronomical Society*, 455, 3735
- Amarsi, A. M., Lind, K., Asplund, M., Barklem, P. S., & Collet, R. 2016b, *Monthly Notices of the Royal Astronomical Society*, 463, 1518
- Angulo, R. E., Springel, V., White, S. D. M., et al. 2012, *Monthly Notices of the Royal Astronomical Society*, 426, 2046
- Anstee, S. D. & O'Mara, B. J. 1991, *Monthly Notices of the Royal Astronomical Society*, 253, 549
- Anstee, S. D. & O'Mara, B. J. 1995, *Monthly Notices of the Royal Astronomical Society*, 276, 859
- Aoki, W., Ito, H., & Tajitsu, A. 2012, *The Astrophysical Journal Letters*, 751, L6
- Arnett, W. D., Meakin, C., Viallet, M., et al. 2015, *The Astrophysical Journal*, 809, 30
- Asensio Ramos, A., Trujillo Bueno, J., Carlsson, M., & Cernicharo, J. 2003, *The Astrophysical Journal Letters*, 588, L61
- Asplund, M. 2005, *Annual Review of Astronomy and Astrophysics*, 43, 481
- Asplund, M., Carlsson, M., & Botnen, A. V. 2003, *Astronomy and Astrophysics*, 399, L31
- Asplund, M. & García Pérez, A. E. 2001, *Astronomy and Astrophysics*, 372, 601
- Asplund, M., Grevesse, N., Sauval, A. J., Allende Prieto, C., & Kiselman, D. 2004, *Astronomy and Astrophysics*, 417, 751
- Asplund, M., Lambert, D. L., Nissen, P. E., Primas, F., & Smith, V. V. 2006, *The Astrophysical Journal*, 644, 229
- Asplund, M., Nordlund, A., Trampedach, R., Allende Prieto, C., & Stein, R. F. 2000, *Astronomy and Astrophysics*, 359, 729
- Asplund, M., Nordlund, A., Trampedach, R., & Stein, R. F. 1999, *Astronomy and Astrophysics*, 346, L17
- Ayres, T. R. & Wiedemann, G. R. 1989, *The Astrophysical Journal*, 338, 1033
- Barklem, P. S. 2016a, *The Astronomy and Astrophysics Review*, 24, 1
- Barklem, P. S. 2016b, *Physical Review A*, 93, 042705
- Barklem, P. S. 2016c, *Zenodo*, 50217
- Barklem, P. S., Belyaev, A. K., & Asplund, M. 2003, *Astronomy and Astrophysics*, 409, L1
- Barklem, P. S., Belyaev, A. K., Dickinson, A. S., & Gadéa, F. X. 2010, *Astronomy and Astrophysics*, 519, A20
- Barklem, P. S., Belyaev, A. K., Guitou, M., et al. 2011, *Astronomy & Astrophysics*, 530, A94

- Barklem, P. S., Belyaev, A. K., Spielfiedel, A., Guitou, M., & Feautrier, N. 2012, *Astronomy and Astrophysics*, 541, A80
- Barklem, P. S. & O'Mara, B. J. 1998, *Monthly Notices of the Royal Astronomical Society*, 300, 863
- Bautista, M. A., Romano, P., & Pradhan, A. K. 1998, *The Astrophysical Journal Supplement Series*, 118, 259
- Becerra, F., Greif, T. H., Springel, V., & Hernquist, L. E. 2015, *Monthly Notices of the Royal Astronomical Society*, 446, 2380
- Behara, N. T., Bonifacio, P., Ludwig, H.-G., et al. 2010, *Astronomy and Astrophysics*, 513, A72
- Bekki, K., Yahagi, H., Nagashima, M., & Forbes, D. A. 2008, *Monthly Notices of the Royal Astronomical Society*, 387, 1131
- Belyaev, A. K. 2013a, *Astronomy & Astrophysics*, 560, A60
- Belyaev, A. K. 2013b, *Physical Review A*, 88
- Belyaev, A. K. 2015, *Physical Review A*, 91, 062709
- Belyaev, A. K. & Barklem, P. S. 2003, *Physical Review A*, 68
- Belyaev, A. K., Barklem, P. S., Dickinson, A. S., & Gad ea, F. X. 2010, *Physical Review A*, 81, 032706
- Belyaev, A. K., Barklem, P. S., Spielfiedel, A., et al. 2012, *Physical Review A*, 85, 032704
- Belyaev, A. K., Yakovleva, S. A., & Barklem, P. S. 2014, *Astronomy and Astrophysics*, 572, A103
- Belyaev, A. K., Yakovleva, S. A., Guitou, M., et al. 2016, *Astronomy and Astrophysics*, 587, A114
- Bensby, T., Feltzing, S., & Oey, M. S. 2014, *Astronomy and Astrophysics*, 562, A71
- Bergemann, M., Collet, R., Amarsi, A. M., et al. 2016, arXiv:1612.07355
- Bergemann, M. & Nordlander, T. 2014, in *Determination of Atmospheric Parameters of B-, A-, F- and G-Type Stars*, ed. E. Niemczura, B. Smalley, & W. Pych, *GeoPlanet: Earth and Planetary Sciences* (Springer International Publishing), 169–185
- Bergemann, M., Ruchti, G. R., Serenelli, A., et al. 2014, *Astronomy and Astrophysics*, 565, A89
- Bessell, M. S., Collet, R., Keller, S. C., et al. 2015, *The Astrophysical Journal Letters*, 806, L16
- B hm-Vitense, E. 1958, *Zeitschrift fur Astrophysik*, 46, 108
- Bromm, V. 2013, *Reports on Progress in Physics*, 76, 112901
- Brook, C. B., Gibson, B. K., Martel, H., & Kawata, D. 2005, *The Astrophysical Journal*, 630, 298
- Brook, C. B., Kawata, D., Gibson, B. K., & Freeman, K. C. 2004, *The Astrophysical Journal*, 612, 894
- Brun, A. S., Turck-Chi eze, S., & Zahn, J. P. 1999, *The Astrophysical Journal*, 525, 1032
- Burkert, A., Truran, J. W., & Hensler, G. 1992, *The Astrophysical Journal*, 391, 651
- Burrows, A. 2013, *Reviews of Modern Physics*, 85, 245
- Carlsson, M., Hansteen, V. H., Gudiksen, B. V., Leenaarts, J., & De Pontieu, B. 2016, *Astronomy and Astrophysics*, 585, A4

- Carlsson, M., Rutten, R. J., & Shchukina, N. G. 1992, *Astronomy and Astrophysics*, 253, 567
- Castelli, F. & Kurucz, R. L. 2004, arXiv:astro-ph/0405087
- Charbonnel, C. & Talon, S. 2005, *Science*, 309, 2189
- Collet, R., Asplund, M., & Trampedach, R. 2006, *The Astrophysical Journal Letters*, 644, L121
- Collet, R., Asplund, M., & Trampedach, R. 2007, *Astronomy and Astrophysics*, 469, 687
- Collet, R., Hayek, W., Asplund, M., et al. 2011, *Astronomy & Astrophysics*, 528, A32
- Cunto, W., Mendoza, C., Ochsenbein, F., & Zeippen, C. J. 1993, *Astronomy and Astrophysics*, 275, L5
- Cyburt, R. H., Fields, B. D., Olive, K. A., & Yeh, T.-H. 2016, *Reviews of Modern Physics*, 88, 015004
- Dobrovolskas, V., Kučinskas, A., Steffen, M., et al. 2013, *Astronomy and Astrophysics*, 559, A102
- Drawin, H.-W. 1968, *Zeitschrift für Physik*, 211, 404
- Dupree, A. K., Avrett, E. H., & Kurucz, R. L. 2016, *The Astrophysical Journal Letters*, 821, L7
- Edvardsson, B., Andersen, J., Gustafsson, B., et al. 1993, *Astronomy and Astrophysics*, 275, 101
- Eggen, O. J., Lynden-Bell, D., & Sandage, A. R. 1962, *The Astrophysical Journal*, 136, 748
- Ezer, D. & Cameron, A. G. W. 1971, *Astrophysics and Space Science*, 14, 399
- Fabbian, D., Khomenko, E., Moreno-Insertis, F., & Nordlund, A. 2010, *The Astrophysical Journal*, 724, 1536
- Fabbian, D., Moreno-Insertis, F., Khomenko, E., & Nordlund, A. 2012, *Astronomy and Astrophysics*, 548, A35
- Feltzing, S. & Chiba, M. 2013, *New Astronomy Reviews*, 57, 80
- Fontenla, J. M., Avrett, E. H., & Loeser, R. 1993, *The Astrophysical Journal*, 406, 319
- Förster, F., Wolf, C., Podsiadlowski, P., & Han, Z. 2006, *Monthly Notices of the Royal Astronomical Society*, 368, 1893
- Frebel, A., Collet, R., Eriksson, K., Christlieb, N., & Aoki, W. 2008, *The Astrophysical Journal*, 684, 588
- Frebel, A., Johnson, J. L., & Bromm, V. 2009, *Monthly Notices of the Royal Astronomical Society*, 392, L50
- Freytag, B., Steffen, M., Ludwig, H. G., et al. 2012, *Journal of Computational Physics*, 231, 919
- Fuhrmann, K. 2004, *Astronomische Nachrichten*, 325, 3
- Gallagher, A. J., Caffau, E., Bonifacio, P., et al. 2016, *Astronomy and Astrophysics*, 593, A48
- Gao, L., Yoshida, N., Abel, T., et al. 2007, *Monthly Notices of the Royal Astronomical Society*, 378, 449
- Gehren, T., Butler, K., Mashonkina, L., Reetz, J., & Shi, J. 2001a, *Astronomy and Astrophysics*, 366, 981
- Gehren, T., Korn, A. J., & Shi, J. 2001b, *Astronomy and Astrophysics*, 380, 645

- Gehren, T., Shi, J. R., Zhang, H. W., Zhao, G., & Korn, A. J. 2006, *Astronomy and Astrophysics*, 451, 1065
- Gilmore, G. & Reid, N. 1983, *Monthly Notices of the Royal Astronomical Society*, 202, 1025
- González Hernández, J. I., Bonifacio, P., Ludwig, H.-G., et al. 2008, *Astronomy and Astrophysics*, 480, 233
- Gratton, R. G., Carretta, E., & Bragaglia, A. 2012, *The Astronomy and Astrophysics Review*, 20
- Gratton, R. G., Carretta, E., Eriksson, K., & Gustafsson, B. 1999, *Astronomy and Astrophysics*, 350, 955
- Greif, T. H., Springel, V., White, S. D. M., et al. 2011, *The Astrophysical Journal*, 737, 75
- Gruyters, P., Korn, A. J., Richard, O., et al. 2013, *Astronomy & Astrophysics*, 555, A31
- Gruyters, P., Lind, K., Richard, O., et al. 2016, *Astronomy & Astrophysics*, 589, A61
- Gruyters, P., Nordlander, T., & Korn, A. J. 2014, *Astronomy & Astrophysics*, 567, A72
- Gustafsson, B., Edvardsson, B., Eriksson, K., et al. 2008, *Astronomy and Astrophysics*, 486, 951
- Hartwig, T., Bromm, V., Klessen, R. S., & Glover, S. C. O. 2015, *Monthly Notices of the Royal Astronomical Society*, 447, 3892
- Hauschildt, P. H., Allard, F., & Baron, E. 1999a, *The Astrophysical Journal*, 512, 377
- Hauschildt, P. H., Allard, F., Ferguson, J., Baron, E., & Alexander, D. R. 1999b, *The Astrophysical Journal*, 525, 871
- Hauschildt, P. H. & Baron, E. 2014, *Astronomy and Astrophysics*, 566, A89
- Hayden, M. R., Bovy, J., Holtzman, J. A., et al. 2015, *The Astrophysical Journal*, 808, 132
- Hayek, W., Asplund, M., Carlsson, M., et al. 2010, *Astronomy and Astrophysics*, 517, A49
- Heger, A. & Woosley, S. E. 2002, *The Astrophysical Journal*, 567, 532
- Heger, A. & Woosley, S. E. 2010, *The Astrophysical Journal*, 724, 341
- Heiter, U. & Eriksson, K. 2006, *Astronomy and Astrophysics*, 452, 1039
- Herwig, F. 2005, *Annual Review of Astronomy and Astrophysics*, 43, 435
- Hinkle, K. H. & Lambert, D. L. 1975, *Monthly Notices of the Royal Astronomical Society*, 170, 447
- Hirano, S., Hosokawa, T., Yoshida, N., Omukai, K., & Yorke, H. W. 2015, *Monthly Notices of the Royal Astronomical Society*, 448, 568
- Hirano, S., Hosokawa, T., Yoshida, N., et al. 2014, *The Astrophysical Journal*, 781, 60
- Holzreuter, R. & Solanki, S. K. 2012, *Astronomy and Astrophysics*, 547, A46
- Holzreuter, R. & Solanki, S. K. 2013, *Astronomy and Astrophysics*, 558, A20
- Holzreuter, R. & Solanki, S. K. 2015, *Astronomy and Astrophysics*, 582, A101
- Howes, L. M., Casey, A. R., Asplund, M., et al. 2015, *Nature*, 527, 484
- Hubeny, I. & Mihalas, D. 2014, *Theory of Stellar Atmospheres*
- Ishiyama, T., Sudo, K., Yokoi, S., et al. 2016, *The Astrophysical Journal*, 826, 9
- Jedamzik, K. & Pospelov, M. 2009, *New Journal of Physics*, 11, 105028
- Johnson, J. L. 2015, *Monthly Notices of the Royal Astronomical Society*, 453, 2771

- Jørgensen, U. G., Johnson, H. R., & Nordlund, A. 1992, *Astronomy and Astrophysics*, 261, 263
- Karakas, A. I. & Lattanzio, J. C. 2014, *Publications of the Astronomical Society of Australia*, 31, e030
- Kaulakys, B. 1991, *Journal of Physics B Atomic Molecular Physics*, 24, L127
- Klevas, J., Kučinskas, A., Steffen, M., Caffau, E., & Ludwig, H.-G. 2016, *Astronomy and Astrophysics*, 586, A156
- Korn, A. J., Grundahl, F., Richard, O., et al. 2006, *Nature*, 442, 657
- Korn, A. J., Grundahl, F., Richard, O., et al. 2007, *The Astrophysical Journal*, 671, 402
- Korn, A. J., Shi, J., & Gehren, T. 2003, *Astronomy and Astrophysics*, 407, 691
- Kroupa, P., Tout, C. A., & Gilmore, G. 1993, *Monthly Notices of the Royal Astronomical Society*, 262, 545
- Kruijssen, J. M. D. 2015, *Monthly Notices of the Royal Astronomical Society*, 454, 1658
- Kurucz, R. L. 1995a, in *Astronomical Society of the Pacific Conference Series*, Vol. 78, *Astrophysical Applications of Powerful New Databases*, ed. S. J. Adelman & W. L. Wiese, 205
- Kurucz, R. L. 1995b, *The Astrophysical Journal*, 452, 102
- Lada, C. J. & Lada, E. A. 2003, *Annual Review of Astronomy and Astrophysics*, 41, 57
- Lambert, J., Josselin, E., Ryde, N., & Faure, A. 2013, in *EAS Publications Series*, Vol. 60, eprint: arXiv:1304.4111, 111–119
- Lambert, J., Josselin, E., Ryde, N., & Faure, A. 2015, *Astronomy and Astrophysics*, 580, A50
- Larson, R. B. 1974, *Monthly Notices of the Royal Astronomical Society*, 166, 585
- Lind, K. 2010, PhD thesis
- Lind, K., Amarsi, A. M., Asplund, M., et al. 2017, *Monthly Notices of the Royal Astronomical Society*, submitted
- Lind, K., Korn, A. J., Barklem, P. S., & Grundahl, F. 2008, *Astronomy and Astrophysics*, 490, 777
- Lind, K., Melendez, J., Asplund, M., Collet, R., & Magic, Z. 2013, *Astronomy & Astrophysics*, 554, A96
- Lind, K., Primas, F., Charbonnel, C., Grundahl, F., & Asplund, M. 2009, *Astronomy and Astrophysics*, 503, 545
- Magic, Z., Collet, R., Asplund, M., et al. 2013a, *Astronomy and Astrophysics*, 557, A26
- Magic, Z., Collet, R., Hayek, W., & Asplund, M. 2013b, *Astronomy and Astrophysics*, 560, A8
- Magic, Z., Weiss, A., & Asplund, M. 2015, *Astronomy and Astrophysics*, 573, A89
- Mashonkina, L., Gehren, T., Shi, J.-R., Korn, A. J., & Grupp, F. 2011, *Astronomy & Astrophysics*, 528, A87
- Massey, H. S. W. 1949, *Reports on Progress in Physics*, 12, 248
- McKee, C. F. & Ostriker, E. C. 2007, *Annual Review of Astronomy and Astrophysics*, 45, 565
- Meléndez, J., Casagrande, L., Ramírez, I., Asplund, M., & Schuster, W. J. 2010a, *Astronomy and Astrophysics*, 515, L3

- Meléndez, J., Ramírez, I., Casagrande, L., et al. 2010b, *Astrophysics and Space Science*, 328, 193
- Michaud, G., Fontaine, G., & Beudet, G. 1984, *The Astrophysical Journal*, 282, 206
- Moore, C. S., Uitenbroek, H., Rempel, M., Criscuoli, S., & Rast, M. P. 2015, *The Astrophysical Journal*, 799, 150
- Nomoto, K., Iwamoto, K., Nakasato, N., et al. 1997, *Nuclear Physics A*, 621, 467
- Nordlander, T., Amarsi, A. M., Lind, K., et al. 2017a, *Astronomy and Astrophysics*, 597, A6
- Nordlander, T., Gruyters, P., Korn, A. J., & Richard, O. 2017b, *Astronomy and Astrophysics*, to be submitted
- Nordlander, T., Korn, A. J., Richard, O., & Lind, K. 2012, *The Astrophysical Journal*, 753, 48
- Nordlander, T. & Lind, K. 2017, *Astronomy and Astrophysics*, submitted
- Norris, J. E., Beers, T. C., & Ryan, S. G. 2000, *The Astrophysical Journal*, 540, 456
- Önehag, A., Gustafsson, B., & Korn, A. 2014, *Astronomy and Astrophysics*, 562, A102
- Pasetto, S., Chiosi, C., Cropper, M., & Grebel, E. K. 2014, *Monthly Notices of the Royal Astronomical Society*, 445, 3592
- Pereira, T. M. D., Asplund, M., Collet, R., et al. 2013, *Astronomy and Astrophysics*, 554, A118
- Pereira, T. M. D., Asplund, M., & Kiselman, D. 2009a, *Astronomy and Astrophysics*, 508, 1403
- Pereira, T. M. D., Kiselman, D., & Asplund, M. 2009b, *Astronomy and Astrophysics*, 507, 417
- Pereira, T. M. D. & Uitenbroek, H. 2015, *Astronomy and Astrophysics*, 574, A3
- Perlmutter, S., Aldering, G., Goldhaber, G., et al. 1999, *The Astrophysical Journal*, 517, 565
- Peterson, R. C. & Schrijver, C. J. 2001, in *11th Cambridge Workshop on Cool Stars, Stellar Systems and the Sun*, Vol. 223, 300
- Piskunov, N. E., Kupka, F., Ryabchikova, T. A., Weiss, W. W., & Jeffery, C. S. 1995, *Astronomy and Astrophysics Supplement Series*, 112, 525
- Planck Collaboration, Ade, P. A. R., Aghanim, N., et al. 2016, *Astronomy and Astrophysics*, 594, A13
- Plez, B., Brett, J. M., & Nordlund, A. 1992, *Astronomy and Astrophysics*, 256, 551
- Prakapavičius, D., Kučinskas, A., Dobrovolskas, V., et al. 2016, *ArXiv e-prints*, 1611, arXiv:1611.03283
- Przybilla, N. & Butler, K. 2004, *The Astrophysical Journal Letters*, 610, L61
- Quinn, P. J., Hernquist, L., & Fullagar, D. P. 1993, *The Astrophysical Journal*, 403, 74
- Reader, J., Kramida, A., & Ralchenko, Y. 2012, in *American Astronomical Society Meeting Abstracts*, Vol. 219, 443.01
- Richard, O., Michaud, G., & Richer, J. 2002a, *The Astrophysical Journal*, 580, 1100
- Richard, O., Michaud, G., & Richer, J. 2005, *The Astrophysical Journal*, 619, 538
- Richard, O., Michaud, G., Richer, J., et al. 2002b, *The Astrophysical Journal*, 568, 979
- Roškar, R., Debattista, V. P., Quinn, T. R., Stinson, G. S., & Wadsley, J. 2008, *The Astrophysical Journal Letters*, 684, L79

- Ruchti, G. R., Fulbright, J. P., Wyse, R. F. G., et al. 2011, *The Astrophysical Journal*, 737, 9
- Rutten, R. J. 2003, *Radiative Transfer in Stellar Atmospheres*
- Ryabchikova, T., Piskunov, N., Kurucz, R. L., et al. 2015, *Physica Scripta*, 90, 054005
- Salpeter, E. E. 1955, *The Astrophysical Journal*, 121, 161
- Samtleben, D., Staggs, S., & Winstein, B. 2007, *Annual Review of Nuclear and Particle Science*, 57, 245
- Sbordone, L., Bonifacio, P., Caffau, E., et al. 2010, *Astronomy & Astrophysics*, 522, A26
- Sellwood, J. A. & Binney, J. J. 2002, *Monthly Notices of the Royal Astronomical Society*, 336, 785
- Shi, J. R., Gehren, T., Butler, K., Mashonkina, L. I., & Zhao, G. 2008, *Astronomy and Astrophysics*, 486, 303
- Short, C. I. & Hauschildt, P. H. 2003, *The Astrophysical Journal*, 596, 501
- Short, C. I. & Hauschildt, P. H. 2005, *The Astrophysical Journal*, 618, 926
- Short, C. I. & Hauschildt, P. H. 2006, *The Astrophysical Journal*, 641, 494
- Soderblom, D. R. 2010, *Annual Review of Astronomy and Astrophysics*, 48, 581
- Spite, F. & Spite, M. 1982, *Astronomy and Astrophysics*, 115, 357
- Springel, V., White, S. D. M., Jenkins, A., et al. 2005, *Nature*, 435, 629
- Steenbock, W. & Holweger, H. 1984, *Astronomy and Astrophysics*, 130, 319
- Steffen, M., Prakapavičius, D., Caffau, E., et al. 2015, *Astronomy & Astrophysics*, 583, A57
- Stein, R. F. & Nordlund, A. 1998, *The Astrophysical Journal*, 499, 914
- Stenholm, L. G. & Stenflo, J. O. 1977, *Astronomy and Astrophysics*, 58, 273
- Stenholm, L. G. & Stenflo, J. O. 1978, *Astronomy and Astrophysics*, 67, 33
- Susa, H., Hasegawa, K., & Tominaga, N. 2014, *The Astrophysical Journal*, 792, 32
- Takeda, Y. & Takada-Hidai, M. 2011, *Publications of the Astronomical Society of Japan*, 63, 547
- Talon, S. & Charbonnel, C. 2008, *Astronomy and Astrophysics*, 482, 597
- Tumlinson, J. 2010, *The Astrophysical Journal*, 708, 1398
- Uitenbroek, H. 2000, *The Astrophysical Journal*, 536, 481
- Unsöld, A. 1955, *Physik Der Sternatmosphären, Mit Besonderer Berücksichtigung Der Sonne*.
- Villalobos, Á. & Helmi, A. 2008, *Monthly Notices of the Royal Astronomical Society*, 391, 1806
- Vogelsberger, M., Genel, S., Springel, V., et al. 2014, *Monthly Notices of the Royal Astronomical Society*, 444, 1518
- Yakovleva, S. A., Voronov, Y. V., & Belyaev, A. K. 2016, *Astronomy and Astrophysics*, 593, A27
- Yoshii, Y. 1981, *Astronomy and Astrophysics*, 97, 280
- Yoshii, Y. 1982, *Publications of the Astronomical Society of Japan*, 34, 365
- Zhao, G., Butler, K., & Gehren, T. 1998, *Astronomy and Astrophysics*, 333, 219

Acta Universitatis Upsaliensis

*Digital Comprehensive Summaries of Uppsala Dissertations
from the Faculty of Science and Technology 1470*

Editor: The Dean of the Faculty of Science and Technology

A doctoral dissertation from the Faculty of Science and Technology, Uppsala University, is usually a summary of a number of papers. A few copies of the complete dissertation are kept at major Swedish research libraries, while the summary alone is distributed internationally through the series Digital Comprehensive Summaries of Uppsala Dissertations from the Faculty of Science and Technology. (Prior to January, 2005, the series was published under the title “Comprehensive Summaries of Uppsala Dissertations from the Faculty of Science and Technology”.)

Distribution: publications.uu.se
urn:nbn:se:uu:diva-313595



ACTA
UNIVERSITATIS
UPSALIENSIS
UPPSALA
2017